Master's thesis

NTNU
Norwegian University of Science and Technology
Faculty of Natural Sciences
Department of Physics

Benedikte Emilie Vindstad

Photosensitizing Effects of Novel Glycosylated Chlorin Complexes on the AY-27 Cancer Cell Model

Master's thesis in Applied Physics and Mathematics

July 2020

NTNU
Norwegian University of
Science and Technology

Photosensitizing Effects of Novel Glycosylated Chlorin Complexes on the AY-27 Cancer Cell Model

BENEDIKTE EMILIE VINDSTAD

Master's Thesis
Trondheim, July 2020

Supervisor:	Professor Mikael Lindgren
Co-supervisor:	Associate Professor Odrun Arna Gederaas

Department of Physics
Norwegian University of Science and Technology

NTNU

Preface

This report is the result of the master's thesis project performed in the final semester of the M. Sc. of Applied Physics and Mathematics program at NTNU. From the day I started my education, I have been particularly interested in the convergence of physics, biology, and medicine. The inherent logic of physics, combined with the incredible complexity of the human body and its processes, fascinates me greatly. Thus, when my supervisor, Prof. Mikael Lindgren, introduced me to the concept of photodynamic therapy - where quantum physics of photons meets the biology of cancer cells - the choice of master's project was made easy.

Throughout our lives, nearly every one of us will experience cancer, ourselves or through a loved one. As a cancer survivor myself, it is my greatest wish to contribute to the field of research which once saved my life. I can think of no better cause, and I am immensely grateful for the introduction into cancer research I have had during this project period.

This work would not be possible without the invaluable guidance of my supervisors at the Department of Physics, Professor Mikael Lindgren and Associate Professor Odrun Arna Gederaas. Thank you for giving me the opportunity to work on this project, for being always available for every question, and for your unrelenting enthusiasm. I also wish to thank Kristin Grendstad, for sharing the joy of cell experiments with me, and for your unwavering support both in and outside the cell lab. Astrid Bjørkøy, thank you for all your help with microscopy and colocalization analysis, and Thor-Bernt Melø, thank you for your assistance and input in the spectroscopy lab. And of course, a special thanks to Prof. Peter Nilsson and Dr. Katriann Arja at Linköping University, for providing the chlorins and making this project possible.

Abstract

The aim of this project was to determine the potential of the KA20 family of glycosylated chlorins as photosensitizers in photodynamic therapy (PDT) of cancer. Cancer is one of the most common causes of death in the world. Because conventional treatments such as chemotherapy and radiotherapy have substantial side effects, it is of interest to explore new treatment modalities. Photodynamic therapy, where a photosensitizer is activated by visible light to kill cancer cells, is one such new treatment. The KA20 family are new potential photosensitizers which may improve the effectiveness of PDT.

To determine the potency of the KA20 chlorins in PDT, rat bladder cancer cell line AY27 were incubated with the compounds. Subsequent illumination with blue light caused a reduction in cell viability of up to 80 % after 60 s and 95+ % after 120 s, relative to untreated cells. Fluorescence imaging confirmed uptake in the cells, and optical measurements confirmed singlet oxygen production. From these results, it was found that the glycosylated KA20 chlorins were effective at causing injury to cancer cells, and that their potential as photosensitizers in photodynamic therapy is present.

Sammendrag

Målet for dette prosjektet var å finne potensialet til KA20-familien av glykosylerte kloriner som fotosensibiliserende forbindelser i fotodynamisk terapi (PDT) av kreftsykdom. Kreft er en av verdens ledende dødsårsaker. Siden konvensjonelle behandlingsmetoder som cellegift og strålesbehandling medfører store bivirkninger, er det av interesse å utforske nye behandlingsmetoder. En slik ny metode er PDT, hvor et fotosensibiliserende stoff aktiveres av synlig lys for å drepe kreftceller. KA20-familien er potensielle nye fotosensibiliserende stoffer som kan forbedre effekten av PDT.

For a bestemme virkningen av KA20-klorinene i PDT ble rotteceller fra blærekreftcellelinjen AY27 inkubert med forbindelsene. Påfølgende belysning med blått lys forårsaket en nedgang i cellenes viabilitet på opp til 80 % etter 60 s og 95+ % etter 120 s, sammenlignet med ubehandlede celler. Fluorescensmikroskopi bekreftet opptak av stoffene i cellene, og optiske målinger bekreftet singlet-oksygenproduksjon. Fra disse resultatene ble det fastslått at de glykosylerte klorinene var i stand til å effektivt gjøre skade på kreftceller, og at de har potensiale som fotosensibiliserende stoffer innenfor PDT.

Acronyms

ALA Aminolevulinic Acid

BER Base Excision Repair

Ce6 Chlorin E6

DNA Deoxyribonucleic Acid

EtOH Ethanol

FBS Fetal Bovine Serum

HRS Hyper-radiosensitivity

IRR Increased Radioresistance

ISC Intersystem Crossing

MCC Mander's Correlation Coefficients

MMR Mismatch Repair

MOC Mander's Overlap Coefficient

NER Nucleotide Excision Repair

PBS Phosphate-buffered Saline

PDT Photodynamic Therapy

PpIX Protoporphyrin IX

PS Photosensitizer

QY Quantum Yield

ROS Reactive Oxygen Species

SD Standard Deviation

SEM Standard Error Of The Mean

SNR Signal-to-noise Ratio

TCSPC Time-Correlated Single-Photon Counting

THF Tetrahydrofuran

Zn-TPP Zinc-tetraphorphyrrin

Contents

Preface i

Abstract iii

Sammendrag v

Acronyms vii

1 Introduction 1

2 Background 7
- 2.1 Principles of Photophysics 7
- 2.2 Mechanisms of Photodynamic Therapy 8
- 2.3 Cell Biology Concepts 13

3 Theory and Methods 17
- 3.1 Optical Spectroscopy 17
- 3.2 Microscopy 22
- 3.3 Colocalization 24
- 3.4 Statistical analysis 32

4 Materials and Methods 35
- 4.1 Chlorins 35
- 4.2 Optical measurements 36
- 4.3 Cultivation of AY-27 cells 38
- 4.4 Cytotoxicity Assay 39

4.5 Photodynamic therapy (PDT) 41
4.6 Fluorescence microscopy 43

5 Results 45
5.1 Overview 45
5.2 Optical measurements 48
5.3 Fluorescence imaging 52
5.4 PDT experiments 54

6 Discussion 57
6.1 Discussion of the results 57
6.2 Evaluation of procedures 65
6.3 Future work 67

7 Conclusions 69
References 71

A Synthetic schemes 81

B Bürker chamber 87

C Images and script used in colocalization analysis 89

D Additional results 95

E Complementary measurements 99

F Comparison of MTT and alamarBlue cell viability assays 105

G LumiSource® lamp 107

Chapter 1

Introduction

Cancer is one of the most common causes of death in the western world. While great strides have been made in the treatment of cancers through chemotherapy, radiotherapy and surgery, the side effects of such treatments can be substantial, and some cancers are resistant to the standard treatments. Recently, interest has increased for new treatment modalities that may be able to treat cancer with fewer side effects than chemotherapy, radiotherapy and surgery. Photodynamic therapy (PDT) is one such treatment modality [1].

PDT is an advanced form of cancer treatment which uses visible light to induce cell death. In PDT, a photosensitizer (PS) is administered to the patient which, after activation by specific wavelengths of light, facilitates production of reactive oxygen species (ROS). The ROS family contains hydrogen peroxide, singlet oxygen and free radicals such as superoxide and hydroxyl radical [2]. These cause a great deal of oxidative stress on cells. This induces malignant cell death, activates antitumor immune response, and damages the vasculature in the tumour.

PDT improves side effects compared to conventional therapy through increased specificity and low systemic toxicity. It achieves this through a dual selectivity. Firstly, the PS can be engineered to have a preference for the diseased cancer cells over healthy cells, promoting accumulation of the drug in the tumour. Secondly, the PS should be minimally toxic to cells unless it is activated by a targeted light source, which can be focused to confine damage to the tumour volume. Together, this means that PDT is able to spare healthy tissue to a greater degree, and thus maintain a low systemic toxicity while still being a non-invasive procedure.

Evidence of the use of light in medicine has been found as far back as ancient Greece [3]. In modern times, the mechanism behind PDT was discovered a hundred years ago [4], but it has only been a subject of serious study since the 1970s. Since then, a few PSs have been approved, and PDT of cancer is in use clinically, though limited to palliative care of various tumour diseases. Though these compounds possess the properties needed for PDT, they also have several acknowledged disadvantages. As an example, Photofrin®, one of the most used PSs, is activated by red light at ca. 630 nm. However, its absorption band in this region is weak, requiring extended illumination from a high-energy source for sufficient activation, which often leads to complications. It is also a very complicated compound that is difficult to synthesise [5]. And lastly, the compound is cleared very slowly from healthy cells, leading to skin photosensitivity in the patient that can persist for weeks or even months. The shortcomings of the current PS options have inspired efforts to develop better alternatives, and there is an ongoing search for new molecular systems for PDT [6, 7, 8]. Recently, novel PSs have been developed from *chlorin* bases, some of which have shown great promise [9].

Purpose of study

This project reports the findings of *in vitro* experiments on a family of seven PSs synthesised from a chlorin base (Table 1.1), developed by Dr. Katriann Arja under the auspices of Prof. Peter Nilsson (Department of Physics, Chemistry and Biology, Linköping University). These compounds were investigated for their effect on rat bladder cancer cell (AY27) cultures. The main objectives of the project were to

- Characterise the photophysical properties of the chlorins,
- Investigate their cell uptake and distribution,
- Compare their efficacy as PSs in PDT.

Due to the COVID-19 pandemic, restrictions were imposed on lab work and presence at the NTNU campus during the project period. Therefore, it was not possible to examine all compounds in detail. A selection was made in order to accomplish a general understanding of the systems, and to carry out the main objectives of the thesis.

Table 1.1: Overview of compounds studied in this thesis. The compounds and their properties were provided by Dr. Katriann Arja, Linköping University. Synthetic schemes and larger images of the chemical structures are included in Appendix A.

Name, chemical formula	Structure	MW [g/mol]	Attached compound
KA20-10.2 $C_{57}H_{42}N_8O_2$	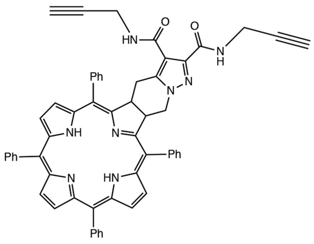	871.02	Alkynes
KA20-11H $C_{73}H_{70}N_{14}O_{14}Zn$	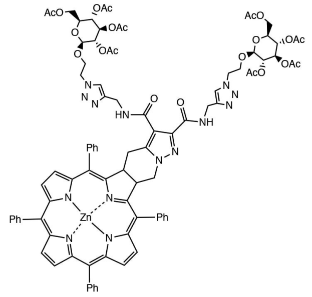	1432.83	Glucose
KA20-11H-proto $C_{73}H_{70}N_{14}O_{14}$	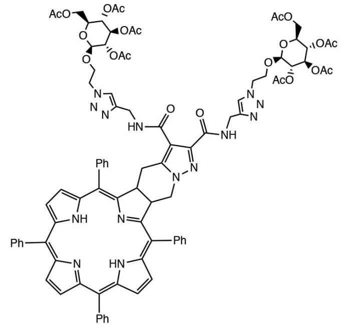	1367.45	Glucose
KA20-15H $C_{73}H_{70}N_{14}O_{14}Zn$	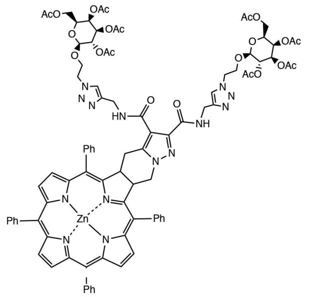	1432.83	Galactose

Continued on next page

Table 1.1 – continued from previous page

Name, chemical formula	Structure	MW [g/mol]	Attached compound
KA20-15H-proto $C_{73}H_{70}N_{14}O_{14}$	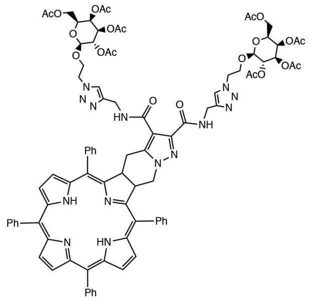	1367.45	Galactose
KA20-16H $C_{77}H_{76}N_{16}O_{14}Zn$	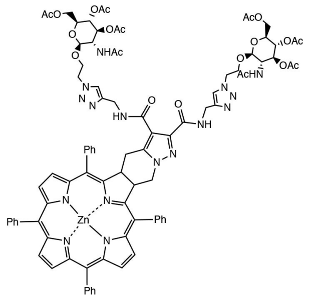	1514.93	N-acetyl glucosamine
KA20-16H-proto $C_{77}H_{76}N_{16}O_{14}$	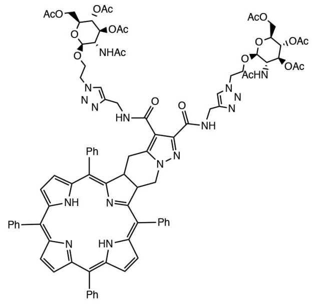	1449.55	N-acetyl glucosamine

Chapter 2

Background

2.1 Principles of Photophysics

Absorption

The absorption of electromagnetic radiation is how matter, especially electrons, take up the energy of a photon, and transforms it into internal energy in the absorber [10]. Quantum mechanical particles such as electrons have discrete values of energy they may inhibit, known as energy states. The electrons of an atom will typically exist in their lowest energy state, known as the ground state. However, they may absorb an incoming photon to temporarily *excite* to higher states (Figure 2.1.1). An excited electron will usually quickly relax back to its ground state by releasing its excess energy.

Emission

One way for an excited electron to relax to its ground state is through the emission of a photon. This is known as luminescence [12]. Luminescence is divided into two categories, *fluorescence* and *phosphorescence*, depending on the nature of the excited state. Fluorescence is emission of photons from the decay of excited *singlet* states, where the excited state electron is of opposite spin to the second electron in the ground-state orbital. Then, the return to the ground state is spin-allowed and occurs rapidly, with a typical *lifetime* of around 1 ns to 10 ns. In phosphorescence, the emission of light comes from *triplet* excited states, in which the excited electron and the remaining ground-state electron have the same spin. This happens when the electron changes

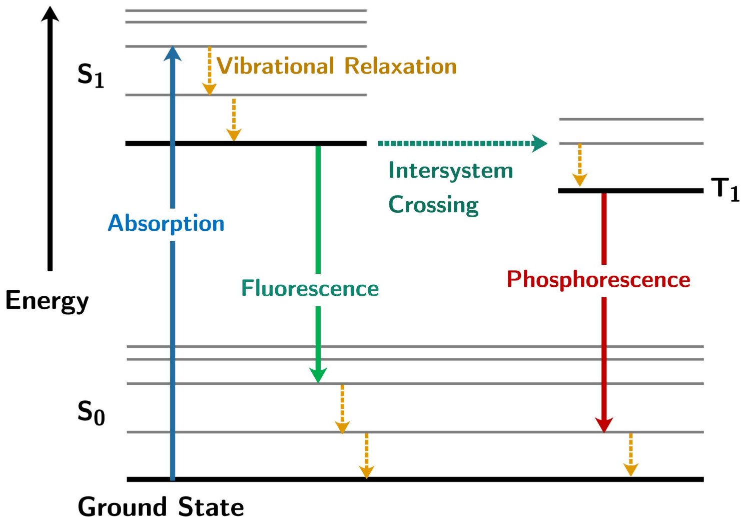

Figure 2.1.1: Absorption, fluorescence and phosphorescence illustrated in a Jablonski diagram. The singlet ground state and first state are shown as black lines denoted by S_0 and S_1, while the triplet first state is denoted by T_1. At each of these, vibrational energy levels may occur, shown as grey lines. The dotted arrows symbolise non-radiative effects. [11]

spin after excitation through intersystem crossing (ISC), as depicted in (Figure 2.1.1). Consequently, the transition back to the ground state is forbidden, causing slow emission rates and lifetimes of the order of microseconds to milliseconds. Therefore, other non-radiant relaxation mechanisms dominate, and phosphorescence is generally rare to observe at room temperature.

2.2 Mechanisms of Photodynamic Therapy

The Photosensitizer

The photosensitizer (PS) in medicine is a drug which is delivered to the patient by intravenous injection or topical application to the skin [1, 5]. Photodynamic therapy (PDT) relies on a dual selectivity, where the cancer cells are targeted both by preferential accumulation of the PS and by the controlled activation of it. The PS selectively targeting the tumour cells can be achieved by exploiting inherent differences between tumour tissues and healthy tissues. For example, tetrapyrroles (such as porphyrins and chlorins), the most widely used PS type, show an inherent preference for tumour cells, thought to be caused by them binding favourably to special proteins displayed by tumour-associated macrophages [13, 14]. In the case of aminolevulinic acid (ALA)-based PDT, the effect is caused indirectly: ALA is one of the precursors in the heme biosynthesis pathway, and by increasing the ALA concentration, the production of the fluorescent protoporphyrin IX (PpIX), the next to last "step" in the pathway, is increased in turn. Here, the produced PpIX compound possesses the photo-sensitising activity. Rapidly proliferating tumour cells tend to exhibit increased enzyme activity in the heme synthesis pathway [15], leading to increased levels of PpIX after ALA incubation compared to healthy tissue [1, 16]. The selectivity of a PS could also be heightened by use of nanomaterials as drug-delivery systems [17], or by conjugating the PS with ligands which target cell-surface receptors over-expressed in tumour cells. Other properties of tumour cells and environments which can be exploited for this purpose include changes in pH and pH regulation [18], disorganised vasculature with increased vascular permeability [19], increased tissue hypoxia [20], and increased glucose metabolism, known as the Warburg effect [21].

After accumulating in the tumour, the PS is then selectively activated in the target cells by shining light of a suitable wavelength on the tumour area. The wavelength needs to be in a range where the PS has an absorption band. However, the possibilities are restricted by the fact that visible light has very short penetration depth in tissue, with deeper penetration at longer wavelengths [22]. To penetrate deep enough, light in the range 600 nm to 1200 nm is needed [23]. However, as wavelengths longer than 800 nm provide too little energy to produce the reactive oxygen species that the therapy relies on to kill the tumour, the window for effective phototherapy lies between 600 nm to 800 nm. This allows for treatment of tumours situated up to 1 cm deep in tissue [24, 25].

To be activated by the light, the PS need to have an absorption band in this red/near-infrared spectral region. Then, photons of a certain suitable energy will excite the PS, allowing it to react with oxygen or biomolecules to create reactive oxygen species.

Reactions with Molecular Oxygen

An excited PS may create reactive oxygen species (ROS) in a cell through two pathways [26]. Firstly, the excited PS may react with biomolecules to form free radicals. The free radicals then further react with *e.g.* molecular oxygen (O_2) to produce ROS such as *e.g.* superoxide, hydrogen peroxide and hydroxyl radical. This process is known as Type 1 reactions. Type 1 reactions include several processes, and do not necessarily involve oxygen and/or the triplet state. Alternatively, the PS may react directly with molecular oxygen to produce singlet oxygen ($^1O_2$) through Type 2 reactions (Figure 2.2.1). When the PS is excited by a photon, it may relax back to the ground state by fluorescence, or it can convert to a triplet state through ISC, as described in section 2.1. When the PS is a triplet state, interaction with singlet-state compounds is forbidden. However, O_2 is one of the very rare compounds to have a triplet ground state, allowing the transfer of energy from the excited PS. The PS relaxes to its ground singlet state, while the oxygen excites to a singlet state, becoming singlet oxygen. Type 1 and Type 2 reactions are illustrated in Figure 2.2.1.

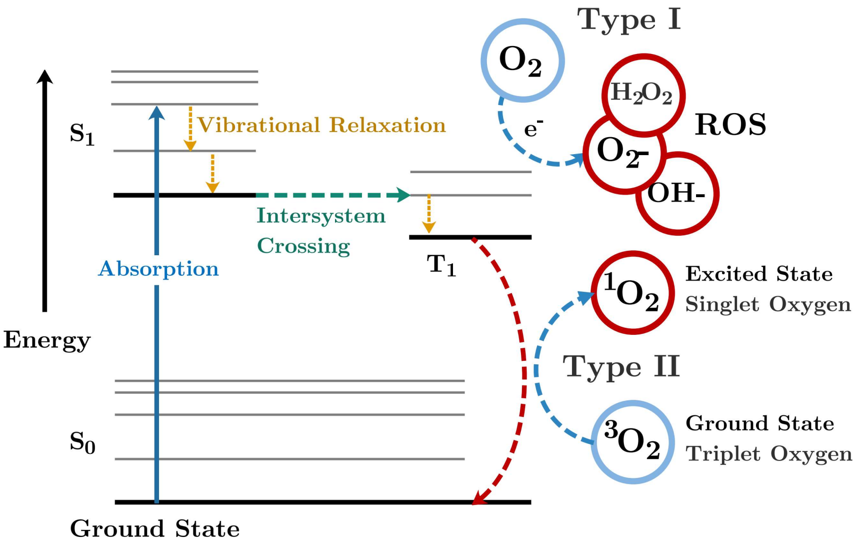

Figure 2.2.1: Creation of ROS illustrated in a Jablonski diagram. The singlet ground state and first state are shown as black lines denoted by S_0 and S_1, while the triplet first state is denoted by T_1. At each of these, vibrational energy levels may occur, shown as grey lines. The dotted arrows symbolise non-radiative effects. Examples of Type 1 reactions and products are depicted, but other variants of these reactions also exist. (Figure drawn by B. Vindstad, 2019)

Both singlet oxygen and other ROS can cause damage to the cell. In addition, various reactive nitrogen species also act together with ROS [27]. However, singlet oxygen is the target of this study, and the discussion will therefore be limited to this species. Singlet oxygen is very reactive and responsible for most of the lesions generated in PDT [26]. In addition, the forbidden nature of the triplet state means that the lifetime of this state is greatly increased compared to the singlet excited state, making a reaction with O_2 more probable. Thus, a high singlet-to-triplet ISC efficiency in the PS is very desirable for PDT.

Antitumor effects of Photodynamic Therapy

The antitumor effects of PDT are three-fold [28]. Firstly, and most importantly, PDT will injure and kill tumour cells through the ROS produced, especially $^1O_2$ [29]. ROS are highly reactive oxygen radicals, and they are able to react with most cellular macromolecules [30]. Thus, they can induce oxidative modifications in proteins, lipids and deoxyribonucleic acid (DNA), all of which are crucial for cellular function. This is known as oxidative stress. ROS are naturally generated in small amounts in the body as a byproduct of metabolic reactions, and cells can counteract some oxidative stress by way of neutralising agents (antioxidants) or repair mechanisms. However, with increased production of ROS, the cell is unable to withstand the increased stress or repair the damage caused, leading to cell damage and cell death.

Due to its high reactivity, singlet oxygen will only be able to diffuse up to 20 nm in a cell before reacting with a biomolecule [26]. Consequently, the intracellular localisation of the damage depends on the localisation of the PS. Through selective localisation, specific organelles such as mitochondria, the plasma membrane, the endoplasmic reticulum or the Golgi complex could be targeted, which could influence the type of cell death induced. For example, PSs which localise to the mitochondria have been found to induce apoptosis to a greater degree than PSs that target other organelles [31, 32].

The second antitumor effect of the therapy is vascular damage. The ROS cause irreversible damage to endothelial cells and the vascular basement membranes in the tumour, leading to haemorrhages in the tissue and the collapse of vasculature [33]. This inhibits the oxygen and nutrient supply in the tumour, which in turn arrests tumour growth and kills tumour cells [34].

Both the above effects will also contribute to the initiation of the third antitumor effect of PDT, which is the triggering of the body's immune system, specifically its inflammation response. The phototoxic damage to the tumour cell membranes trigger the local production of proinflammatory cytokines and chemokines. These, in turn, trigger the accumulation of neutrophils and other inflammatory cells at the site, which attack the tumour cells [34, 35].

Singlet oxygen and DNA damage

All four bases of DNA are susceptible to oxidative damage from $^1O_2$ and other ROS, due to their highly reactive nature. However, of the four, guanine has the lowest reduction/oxidation potential and is therefore more susceptible to oxidation [36]. 8-oxo-7,8-dihydro-20-deox-yguanosine (8-oxodG) has been identified as one of the main products of the reaction of $^1O_2$ with DNA, but multiple other products may be formed, and $^1O_2$ may react further with 8-oxodG to form other final products as well [37]. This damage has been found to directly affect several enzymes of the cell core metabolism, and been shown to cause mutagenesis in the cell [38], especially G to T transversions [37]. Such mutations in DNA may decrease the viability of the cell, and may cause cell death or permanent arrestation.

2.3 Cell Biology Concepts

The Cell Cycle

The cell cycle is an ordered series of events in which the cell grows, duplicates its DNA, and divides, creating two daughter cells [39]. The growth and DNA replication takes place in the *interphase*, while the act of division is denoted the *mitotic phase*. Interphase is further divided into three subphases: G_1-phase, where the cell grows and accumulates energy, S-phase, where the DNA synthesis takes place, and G_2-phase, where the cell replenishes its energy stores and prepares for mitosis. Cells at different stages may be distinguished by the amount of DNA present in their nucleus. The cycle is illustrated in Figure 2.3.1.

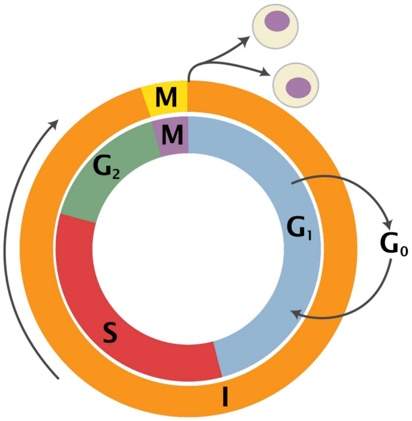

Figure 2.3.1: Schematic representation of the cell cycle. Outer ring: I = Interphase, M = Mitosis; inner ring: M = Mitosis, G1 = Gap 1, G2 = Gap 2, S = Synthesis; not in ring: G0 = Gap 0/Resting. Figure by Richard Wheeler, Wikimedia Commons, 2006 [40].

At several points in the cell cycle, checkpoints function to ensure proper division of the cell into viable daughter cells. If DNA damage is detected at the checkpoints, the cells' progression through the cycle is arrested until the damage is repaired [39]. One of the most clearly defined checkpoints is the G_2-phase checkpoint, which prevents progression to M-phase if the DNA replication is incomplete, but many other checkpoints exists throughout the cell cycle [41].

DNA damage repair

DNA damage is an abnormal alteration in the DNA structure that may cause cellular injury or reduce the viability of the cell [42]. DNA damage may be intentionally inflicted through cancer treatments such as radiation, chemotherapy and PDT, but also occurs naturally through normal metabolic activity. Thus, a number of pathways to localise and repair these lesions have evolved. In a healthy cell, repair pathways keep the cell viable and prevent mutations in the genomic material which may lead to cancer. In cancer therapy, the repair pathways are an obstacle, as they allow the cancer cell to resist the treatment by repairing the damage inflicted.

DNA damage may take the form of abnormal alterations to a base site. Alternatively, single strand breaks (SSB) and double strand breaks (DSB) may occur, where one or both strands of the helix are cleaved. Each type of damage requires different repair strategies. As discussed in section 2.2, the main interaction of ROS such as $^1O_2$ and DNA is the oxidation of bases, especially guanine, causing the DNA strands to be altered but unbroken. The main DNA repair pathways implicated in the correction of such lesions are nucleotide excision repair (NER), base excision repair (BER) and mismatch repair (MMR). Of these, BER is thought to be the main pathway for oxidative damage. In this process, the position of the damaged base is signaled, and repair proteins are recruited to the site. The affected base is excised and removed, followed by renewal by transcription using the undamaged opposite strand as blueprint. This results in complete repair of the damage, preventing mutagenesis such as G to T transversions [37].

Modes of cell death

If not repaired, damage caused to the cell may lead to cell death through two main pathways: apoptosis or necrosis. Apoptosis is a programmed form of cell death, meaning it is initiated and regulated by the cell. Cell death through apoptosis happens naturally as a part of numerous physiological processes in the body, but may also be provoked by malignant circumstances, such as in cancer treatment [43]. Apoptotic cell death morphology includes cell shrinkage and membrane blebbing, followed by formation of small, membrane-enclosed apoptotic bodies containing the organelles of the cell. These bodies may then be phagocytosed and digested by neighbouring cells. This process, in contrast to necrosis, is a natural death for a cell, and thus does not trigger any inflammatory response in the body.

Necrosis, on the other hand, is the death of a cell as a consequence of external factors such as toxins, trauma and infection. Necrotic cells will swell rapidly. The internal structures of the cell, such as the nucleus, become fragmented, followed by the plasma membrane collapsing. The membrane, cytoplasmic structures and nucleus will

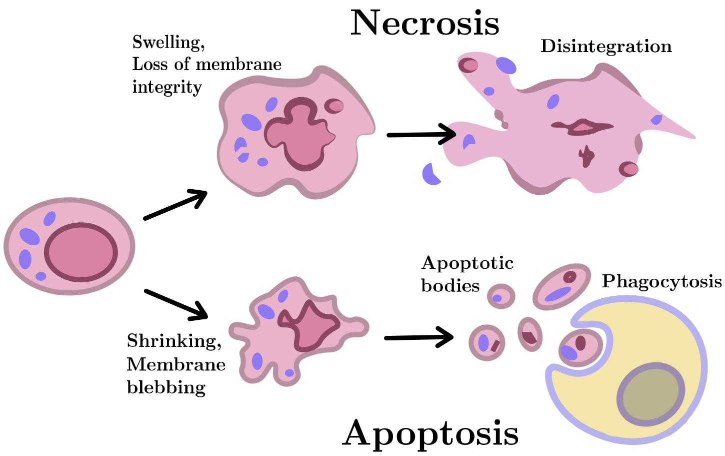
Necrosis
Swelling,
Loss of membrane
integrity
Disintegration
Apoptotic
bodies
Phagocytosis
Shrinking,
Membrane
blebbing
Apoptosis

Figure 2.3.2: Illustration of the structural changes of cells undergoing necrosis and apoptosis. (B. Vindstad, 2019)

dissolve, and fragmented DNA strands, proteins and organelles leak into the environment. The release of these products of cell death into the extracellular space triggers an inflammation response in the tissue [44]. Apoptosis and necrosis are illustrated in Figure 2.3.2.

Chapter 3

Theory and Methods

3.1 Optical Spectroscopy

Both the spectral and temporal properties of a luminescent molecule can change depending on its surroundings (polarity, viscosity, pH etc.). From basic spectroscopy measurements (absorbance, luminescence and lifetime), one can ensure that a molecular system is acting as expected, which allows for comparisons with similar systems in literature. Besides, many spectral parameters can be measured using a fluorescence microscope at various positions, *e.g.* in a cell. Therefore, it is useful to know these basic properties of the systems prior to microscopy investigation. This section describes the theory behind optical measurements performed in this project.

Absorption Spectroscopy

The *absorbance* of a material characterises the amount of radiation absorbed in relation to the amount of radiation received. The absorbance A of a material is given by [45]:

$$A = \log_{10}\left(\frac{\Phi_i}{\Phi_t}\right) \tag{3.1.1}$$

where Φ_i denotes the radiant flux *received* and Φ_t denotes the radiant flux *transmitted* by the material. The *Beer-Lambert law* relates the absorbance of a material to its concentration c, its molar attenuation coefficient ϵ, and the path length l of the light through the material [45]:

$$A = \epsilon c l \tag{3.1.2}$$

As seen in Figure 2.1.1, an electron will have discrete quantum mechanical energy levels to which it can be excited. Absorption of radiation to excite the electron is more likely when the incoming photons' frequencies correspond to the energy difference between two states. Consequently, the absorbance of a material changes depending on the wavelength of the incident light. In a spectrophotometer, the absorbance for a range of wavelengths may be measured, and the absorption spectrum can be found.

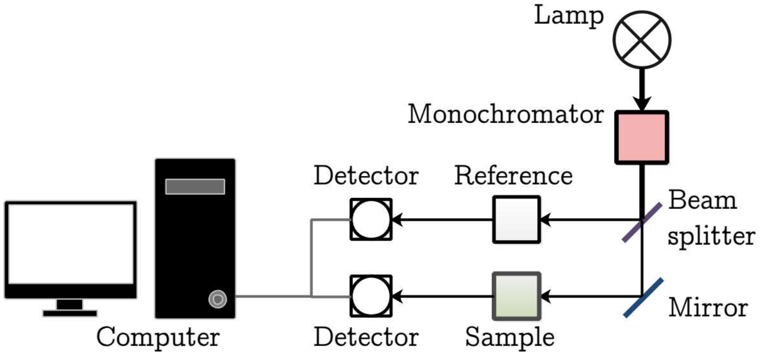

Figure 3.1.1: Schematic setup of a double beam absorption spectrophotometer. (Figure drawn by B. Vindstad, 2019)

In Figure 3.1.1, the setup for a double beam absorbance spectrophotometer is illustrated. Radiation of different wavelengths is sequentially applied to a dissolved sample, contained in a glass cell. A monochromator ensures that only a single wavelength is applied to the sample at a time. A detector measures the light transmitted through the sample. The absorbance is then found from equation (3.1.1). This value is the sum of the absorption of the glass, the solvent and the molecule of interest:

$$A_{total} = A_{material} + A_{solvent} + A_{cell} \tag{3.1.3}$$

In order to isolate the absorbance of the sample, a reference measurement of an equivalent glass cell containing solvent only is measured simultaneously. When the absorbance value of the reference is subtracted from the one of the sample, the absorbance spectrum of the material only is obtained.

There are alternative techniques to measure an absorption spectrum. Using an array detector, a full spectrum can be measured in one instance. This requires a broad band light source. In order to set the absorbance A in equation 3.1.1, the spectrum must be recorded twice, with and without solute. This technique is useful for transient experiments.

Luminescence Spectroscopy

Measuring the number of emitted photons as a function of wavelength results in an *emission spectrum* [12]. As can be seen from the Jablonski diagram (Figure 2.1.1), relaxation from a higher to a lower vibrational state within the same electronic state does not emit a photon. Typically, vibrational relaxation in fluorescence happens very rapidly, dissipating the excess energy and leaving the electron in the lowest vibrational level of S_1 before relaxation to the ground state, no matter the absorbed energy. Also, the electron may relax to a higher vibrational state within the ground state. This causes the emitted photons to typically be of lower energy than the photons absorbed to excite the electron. The emission spectrum will thus be shifted towards longer wavelengths compared to the absorption spectrum. Importantly, it will also generally be independent of the excitation wavelength.

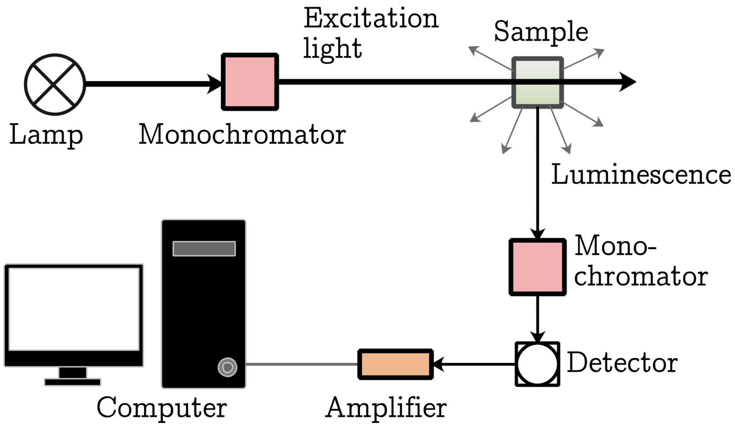

Figure 3.1.2: Schematic setup of a luminescence spectrophotometer. (Figure drawn by B. Vindstad, 2020)

The emission is usually measured using a 90° configuration (Figure 3.1.2) to reduce the background signal from the excitation source. Therefore, luminescence spectroscopy is very sensitive, and single photons can be detected.

Quantum Yield

The quantum yield (QY) of a fluorophore is the number of photons emitted relative to number of photons absorbed. The QY depends on the fraction of fluorophores which decay through emission versus through nonradiative decay [12]:

$$Q = \frac{\Gamma}{\Gamma + k_{nr}} \tag{3.1.4}$$

Here, Γ denotes the emissive rate constant, and k_{nr} the rate constant of all nonradiative decay processes, grouped together. The QY may be close to unity if the radiationless decay rate is much smaller than the rate of radiative decay.

The QY of a sample may be found through comparison to a different compound with known QY values. The relative QY of two samples is given by

$$\frac{\Phi_X}{\Phi_{Ref}} = \frac{A_{Ref}}{A_X} \cdot \frac{F_X}{F_{Ref}} \cdot \frac{n_X^2}{n_{Ref}^2} \tag{3.1.5}$$

Where 'X' denotes an unknown sample and and 'Ref' a known reference sample (see *e.g.* K. Rurack and M. Spieles, 2011 [46]). A is the absorbance at the excitation wavelength, F is the corrected integrated fluorescence spectrum, and n is the refractive index of the solvent. By measuring and integrating the fluorescence spectra for several absorbance values for each sample, a linear relationship can be found. The gradient of the linear fitted equation is then given by

$$\text{Grad}_i = \frac{\Delta F_i}{\Delta A_i}, \tag{3.1.6}$$

reducing 3.1.5 to

$$\frac{\Phi_X}{\Phi_{Ref}} = \frac{\text{Grad}_X}{\text{Grad}_{Ref}} \cdot \frac{n_X^2}{n_{Ref}^2} \tag{3.1.7}$$

from which the unknown QY value can be calculated.

Fluorescence Lifetime

A fluorophore which is excited by a photon will relax back down to the ground state with a certain probability, based on the decay rates of the different available pathways. The fluorescence emitted will decay exponentially [12]:

$$I(t) = I_0 e^{-t/\tau} \tag{3.1.8}$$

The fluorescence *lifetime* τ is the average time the molecule spends in the excited state before returning to the ground state. τ is given by:

$$\tau = \frac{1}{\Gamma + k_{nr}} \tag{3.1.9}$$

The lifetime is usually measured with a configuration such as in Figure 3.1.2.

The lifetime is not only important to assess the nature of the luminescence (fluorescence vs. phosphorescence as depicted in Figure 2.1.1), but is also a sensitive monitor of the environment of a luminescent molecule [47]. Dynamic polar groups usually shorten the lifetime, whereas hydrophobic unpolar environments extend the lifetime. Special fluorescent molecules may be designed to report such molecular properties in proteins, membranes and various cellular compartments [12].

3.2 Microscopy

Bright and Dark Field Microscopy

Bright-field microscopy is the simplest form of optical microscopy [48]. High-intensity light is emitted by an illuminator and focused onto the sample by a condenser lens. The light from the illuminator is transmitted, absorbed, reflected or refracted by the sample depending on its properties, and the image is collected and magnified through objective lenses and the ocular lenses of the eyepiece. The result is a bright background image with the structures of the specimen appearing darker, depending mainly on their thickness, density and light absorption.

In dark-field microscopy, a small, opaque disk is placed between the illuminator and the condenser lens. The disk stops most of the light from reaching the sample, leaving only a hollow cone of focused light. The light in this cone is not collected by the objective lens unless it is refracted or reflected by structures in the specimen. The result is bright objects on a dark background image, which enhances the contrast for weakly absorbing samples.

Fluorescence Microscopy

Fluorescence microscopy is used to image fluorochromes in a sample. Excitation light of wavelengths absorbed by the fluorochrome is transmitted to the sample, and the resulting fluorescence is collected. The excitation light is filtered out, so that only the fluorescence passes through the ocular lens. This produces an image with the fluorochrome visible in bright colors against a dark background. This is the most sensitive form of optical microscopy, and single emitters can be detected by repeated measurement using a pulsed laser.

Confocal Laser Scanning Microscopy (CLSM)

The *confocal* approach to fluorescence microscopy is the use of spatial filtering techniques to eliminate signal from outside the focal plane [49]. This way, one can capture two-dimensional images from different depths, known as optical sections, from specimens whose thickness exceeds the plane of focus. A confocal microscope achieves this by the use of *point illumination*. In traditional wide-field fluorescence microscopy, the entire specimen is evenly illuminated and all parts of the sample is excited at the same time. The resulting fluorescence detected in the microscope thus includes a a large amount of unfocused background light. Confocal laser scanning microscopes focus the laser at the focal plane, limiting the volume of the specimen receiving excitation light, and block out any out-of-focus fluorescence by using a pinhole in an optically conjugate plane in front of the detector. This greatly increases the axial resolution compared to wide-field microscopes at the cost of decreased signal intensity. To offset the drop in signal, CLSM microscopes utilise very sensitive detectors to acquire the light intensity, usually photomultiplier tubes.

3.3 Colocalization

One application of fluorescence microscopy is to see the subcellular distribution of molecules [50]. To achieve this, antibodies and other molecules which bind to certain organelles or biomolecules with high specificity may be marked with fluorescent dyes. The fluorescence from these dyes may then be used to localise the molecule in the sample, which in turn localises the organelle to which it binds. In this way, the fluorescent dye is used to visualise the target biomolecule. Alternatively, the signal from the dye can be compared to other fluorophores present in the cell, and used to help determine their distribution among the organelles. As an example, if signal from a fluorophore overlaps, or *colocalizes*, with signal from a dye which stains mitochondria, this may indicate that the fluorescent molecule has a preference for mitochondria as well. An example of a cell stained with different dyes is shown in figure 3.3.1.

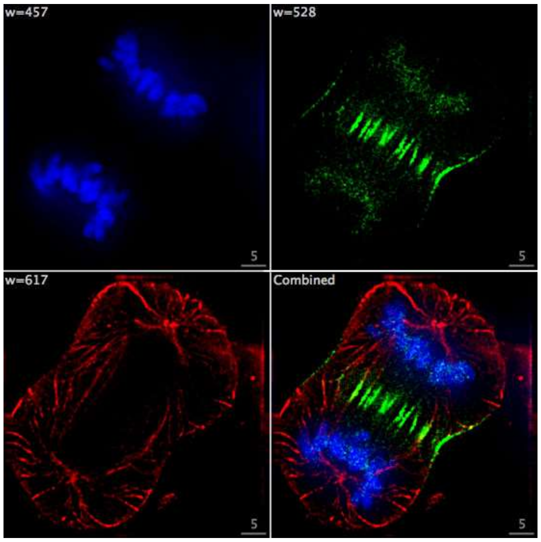

Figure 3.3.1: An image of a human cancer cell dividing. The cell is fixed and imaged in an epifluorescence microscope. DNA is stained blue, centromeres green, and microtubules red. Image by F. Lamiot, Wikimedia Commons, 2010 [51].

In order to measure this colocalization, several different approaches are possible. The easiest, and most used, is to simply create an overlay image of *e.g.* the red and green channels, and visually assess the amount of yellow pixels in the combined image [52]. This method is quick and straightforward, but may be misleading. Intermediate colour can only be obtained if the intensities of the signal from the fluorophores are similar. Even small changes in the relative intensity of two probes can completely alter the combined colour in the overlay image, and impact the perception of colocalization

[50]. Therefore, the degree of colocalization is visually apparent in this way only under very specific labeling conditions, where fluorescence of the different probes occurs in equal proportion. This section will present some of the methods available to quantify colocalization in fluorescence images.

Correlation vs. co-occurrence

What is collectively referred to as colocalization analysis actually consists of two disinct sets of methods. These measure two separate phenomena: *Co-occurrence* or *correlation* [53]. Co-occurrence describes the extent of the spatial overlap between two fluorophores, while correlation describes the degree to which the abundance of two spatially overlapping fluorophores are related. The difference is illustrated in figure 3.3.2. Co-occurrence measurements can be used to determine what proportion of a probe is present in a particular area, but does not give any information on concentration relationships between two probes. Correlation can be used to find functional relationships between two overlapping probes, but does not measure their spatial co-occurrence. Neither are direct measurements of molecular interaction.

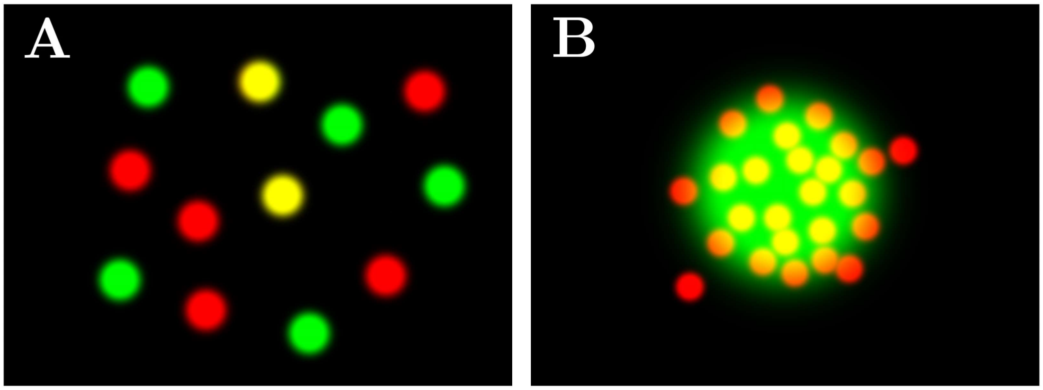

Figure 3.3.2: Correlation vs. co-occurrence. A: An example of high correlation (PCC = 0.99) and low co-occurrence (MOC = 0.22). B: An example of high co-occurrence (MOC = 0.68) and low correlation (PCC = 0.1). POC and MOC are defined in equation 3.3.5 and 3.3.2. (B. Vindstad, 2020)

For the fluorescence images used in this thesis, the co-occurrence of PSs and labelling dyes were of greatest interest. Therefore, only methods determining this property were utilised. However, for completeness, methods for both properties and their uses will be explored in the following sections.

Co-occurrence: Area analysis

The simplest method for co-occurence analysis is to measure the area of the overlap between the signals of interest. In this calculation, intensity values above a certain threshold are set to one, while the rest of the signal is set to zero, dividing the image into binary areas of signal or no signal. This process is illustrated in figure 3.3.3. The signal area overlap, or intersection, from two channels may then be expressed as a percentage of the total (union) area:

$$\text{Overlap percentage} = \frac{A_{intersection}}{A_R + A_G - A_{intersection}} \times 100 \tag{3.3.1}$$

Where A_R designated the area of red signal (visualised in 3.3.3D), A_G designated the area of green signal (3.3.3E), and $A_{intersection}$ designates the union area of both green and red signal (3.3.3F).

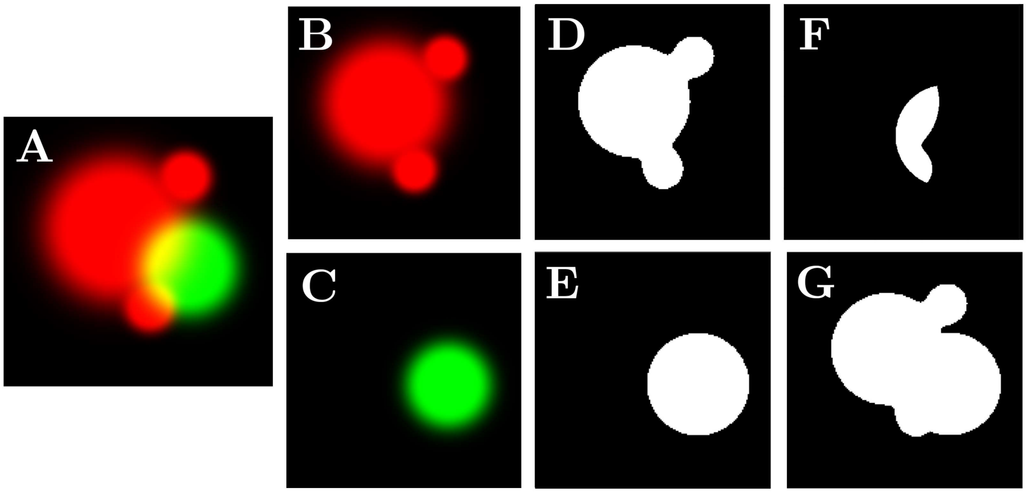

Figure 3.3.3: An illustration of simple area analysis. A: Image consisting of two channels, separated in B and C. D, E: A binary threshold is applied to the red and green channels. F: The intersection area of the two channels. G: The union area of the two channels. By dividing the area of F by the area of G, the overlap for this image is found to be 15 %. (B. Vindstad, 2020)

As simple area analysis is an intuitive and easily implemented method to measure co-occurrence, this is one of the methods used for the colocalization analysis in this thesis. This method is quick, simple and the resulting percentage value is easy to interpret. However, all information on differing intensities, or the abundance of the probes, is discarded when the binary threshold is applied. In situations where the relative concentrations of probes are of interest, other methods should be used. Finding the appropriate threshold value can also be a challenge, and is susceptible to user bias if done manually. Thresholds appear in other methods, as well, and are discussed further later in this section.

Co-occurrence: Mander's Overlap Coefficient

One alternative metric is Mander's overlap coefficient (MOC). For a red/green channel image, MOC is given by [54]:

$$\mathrm{MOC} = \frac{\sum_i (R_i) \times (G_i)}{\sqrt{\sum_i (R_i)^2 \times \sum_i (G_i)^2}} \tag{3.3.2}$$

Here, R_i and G_i refer to the i^{th} above-threshold pixel value in the red and green channels, respectively.

MOC takes into account the difference of intensities in the overlapping pixels, giving more weight to higher intensities. This preserves more information compared to simple area analysis. MOC is also robust against the effect of an increasing signal-to-noise (SNR) ratio. However, the coefficient is strongly influenced by the ratio of the number of pixels in each channel. This means that MOC is more accurate for images with roughly equal numbers of red and green pixels, which limits its usefulness. It is also sensitive to out-of-focus signal and other unwanted signal sources, as these increase pixel intensity and inflate the MOC value.

It is sometimes of more interest to quantify the *fraction* of one probe that co-occurs with a second probe. For this purpose, MOC may be divided into Mander's correlation coefficients (MCC). For two probes R and G, two MCC values are derived, M_1 and M_2 [54]:

$$\mathrm{M}_1 = \frac{\sum_i R_{i,colocal}}{\sum_i R_i} \qquad R_{i,colocal} = \begin{cases} R_i & \text{if } G_i > 0, \\ 0 & \text{if } G_i = 0, \end{cases} \tag{3.3.3}$$

$$\mathrm{M}_2 = \frac{\sum_i G_{i,colocal}}{\sum_i G_i} \qquad G_{i,colocal} = \begin{cases} G_i & \text{if } R_i > 0, \\ 0 & \text{if } R_i = 0, \end{cases} \tag{3.3.4}$$

This simply gives the fraction of total R fluorescence that is found in pixels where G fluorescence is present, and *vice versa*. This "split" coefficient for co-occurrence is a better fit for images where the two probes are present in differing amounts, as is the case for the images studied in this thesis. Therefore, Mander's correlation coefficients

(MCC) were used in addition to simple area analysis for colocalization analysis in this project.

Correlation: Pearson's Correlation Coefficient

To quantify correlation of two probes, Pearson's correlation coefficient (PCC) can be used. PCC compares the deviation from the mean intensity for each colour in each pixel. For an image consisting of red and green channels, PCC is given by

$$\mathrm{PCC} = \frac{\sum_i (R_i - \overline{R}) \times (G_i - \overline{G})}{\sqrt{\sum_i (R_i - \overline{R})^2 \times \sum_i (G_i - \overline{G})^2}} \tag{3.3.5}$$

where R_i and G_i refer to the intensity values of the red and green channels in pixel i, and $\overline{R}$ and $\overline{G}$ refer to the mean intensities of the red and green channels across the entire image [55]. PCC values range from 1 to -1, where a value of 1 represents perfectly linearly related red/green fluorescence intensities, or complete colocalization, and -1 represents images whose fluorescence intensities are perfectly inversely related, or complete exclusion. Values near zero reflect uncorrelated signal. The relationships between the red and green intensities are visualised in scatterplots in figure 3.3.4.

The main advantage of PCC is its simplicity and the fact that it is independent of signal level and signal offset [50], as the mean intensity is subtracted from each pixel's intensity values. However, the coefficient has some major drawbacks. Since the deviation from the mean signal is evaluated, PCC is sensitive to differences in intensities from different components in the image. Therefore, PCC may be inaccurate for an image with cell-cell or organelle variability in probe intensity. The measurement is sensitive to noise, and can be artificially inflated by the presence of background pixels. These seemingly empty areas will contain some red and green signals significantly below their average levels, which is interpreted as colocalization. Therefore, regions of interest should be identified before analysis, which can be complicated and time-consuming, and it might not be possible to account for all empty intracellular regions. Lastly, while the meaning of PCC values near 1 and -1 are generally clear, intermediate values, in particular negative ones, can be difficult to interpret.

Also, PCC increases when the scatterplots of the pixel intensity of two images are linearly related. However, in some cases, the correlation may be present but non-linear. In these situations, PCC will underestimate the correlation. To address this issue, Spearman's rank correlation coefficient (SRCC) can be used [56]. SRCC is equivalent to PCC, but applied to pixel intensity *ranks* as opposed to the intensities themselves. The lowest pixel intensity is assigned a rank of 1, the second lowest a rank of 2, *et cetera*. If multiple pixels have the same intensity, that value is assigned an average rank. This linearizes the scatterplots, so that the correlation coefficient becomes applicable.

Correlation: Li's approach

Another method to quantify correlation is Li's approach [57][58]. First, assume that the variations from the mean intensity for each channel sums to zero: $\sum_i (R_i - \overline{R}) = 0$ and $\sum_i (G_i - \overline{G}) = 0$. Then, for two sets with random staining intensities, the product of these equalities should tend to zero. However, in the case of correlation, the intensity of both channels will vary in the same direction relative to their respective mean intensity values. Thus, $(R_i - \overline{R})$ and $(G_i - \overline{G})$ will more often be of the same sign, and the sum of their product will tend to a positive value. Likewise, anti-correlation will cause the variations to be of opposite signs more often, leading to a negative product value. When the intensities of R and G are plotted as a function of the $(R_i - \overline{R}) \times (G_i - \overline{G})$, random distributions will have a roughly equal amount on either side of the $x = 0$ line, dependent distributions will have a majority on the positive side, and segregated distributions will have a majority on the negative side. This is illustrated in figure 3.3.4.

The correlation found from this analysis may be expressed by the intensity correlation quotient (ICQ), where the amount of pixels on the positive side of the plot is simply divided by the total number of pixel pairs. To distribute the quotients in the -0.5 to 0.5 range, 0.5 is subtracted from this value. Then, random staining gives ICQ $\simeq 0$, correlation gives $0 <$ ICQ ≤ 0.5 and anti-correlation gives $0 >$ ICQ ≥ -0.5.

The Costes method for threshold determination

For the methods discussed above, it is of importance to separate the background pixels from the signal pixels. Most are products of signal intensities, so that pixels where one or both channels have zero value are not included. However, the value of background pixels in fluorescence images are rarely actually zero, as they may contain signal from light leakage, autofluorescence, out-of-focus fluorescence, or from a positive offset in the detector stage. The easiest method for eliminating this background signal is to set all pixels below a threshold value to zero, as is done in simple area analysis. However, finding the appropriate threshold value may be challenging, especially for images where the probe signal occurs in structures with fluorescence intensity similar to that of the background. For these images, the resulting quotients can be sensitive to even small changes in the threshold value. Thus, with a manual threshold process, the result is

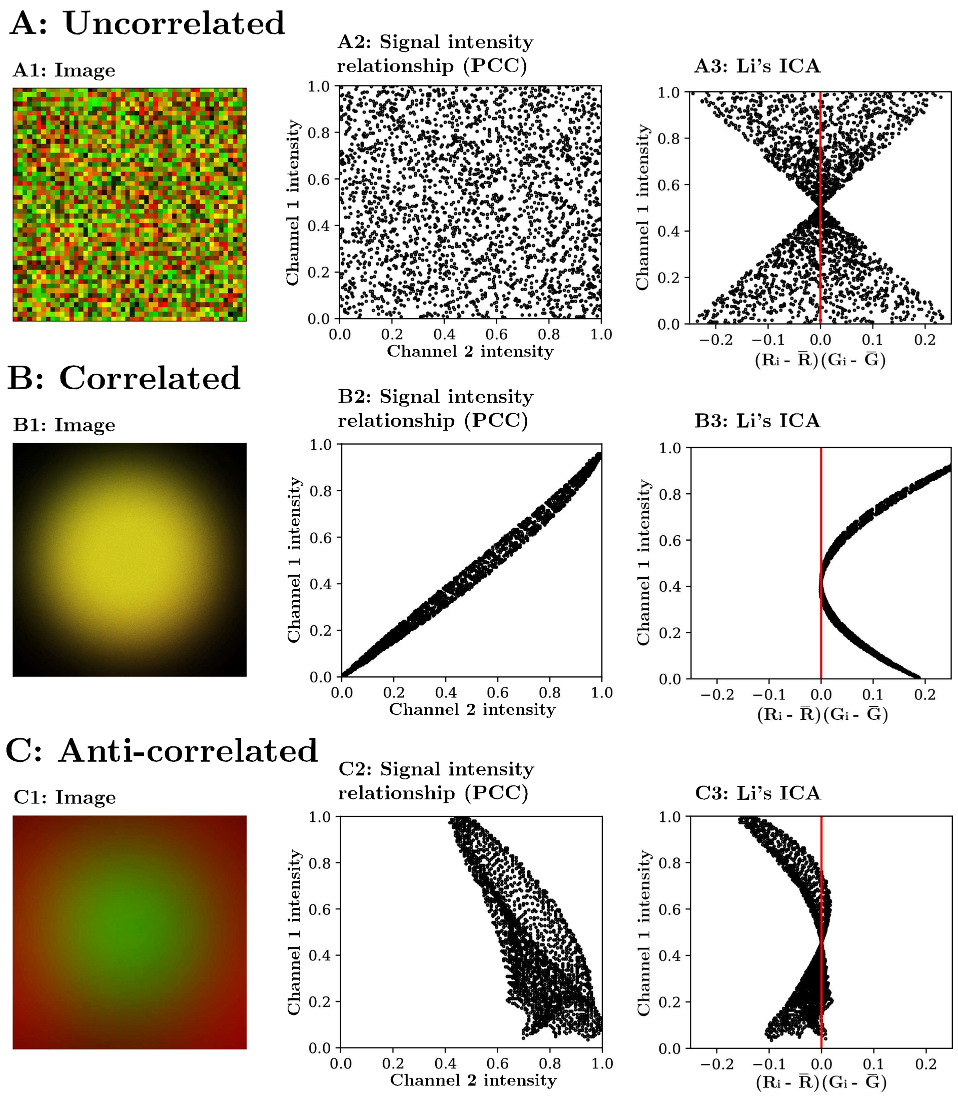

Figure 3.3.4: An illustration of the relationships between signal intensity and Li's intensity correlation analysis for two channel images.
A: Random distribution of red and green values. The plot of green vs red pixel intensities show no relationship. Li's ICA gives equal amounts on either side of x = 0.
B: A dependent distribution of red and green values. The plot of green vs red intensities show a clear linear relationship. Li's ICA shows a majority on the right side of x = 0.
C: An inversely related distribution of red and green values. The plot of red vs green intensities show a negative linear relationship. Li's ICA shows a majority on the left side of x = 0.
(Figure by B. Vindstad, 2020)

vulnerable to user bias, and may vary depending on the person deciding the threshold value.

In order to avoid this subjectivity, Costes' method for automatic threshold determination can be used [59]. By iteratively calculating the PCC for different threshold values, this method determines the thresholds for which the PCC for the pixels below the thresholds equals zero. Then, the pixels above the threshold have correlation > 0, while the pixels below the threshold have none or anti correlated intensities. The Costes method is fully reproducible, and will yield similar threshold for similar datasets, eliminating the unreliability of manual thresholding.

While automatic threshold determination would lead to greater dependability for the colocalization analysis, Costes' method was not implemented in this project due to time limitations. Instead, thresholds were set manually for each image.

3.4 Statistical analysis

This section details the statistical methods utilised in analysis of the data gathered in the thesis. The specific methods used for each data set are denoted in figure legends in the Results section.

Standard error

The standard deviation (SD) is a measure of the amount of variation within a set of values. The SD of a sample may be estimated by

$$\sigma \approx \sqrt{\frac{1}{N-1}\sum_{i=1}^{N}(x_i-\overline{x})^2} \tag{3.4.1}$$

where $x_1, x_2, ..., x_N$ are the observed values, $\overline{x}$ is the mean value of the observed values, and N is the number of observations in the sample.

The standard error of the mean (SEM) can be found from the SD:

$$\sigma_{\overline{x}} = \frac{\sigma}{\sqrt{N}} \tag{3.4.2}$$

where $\sigma_{\overline{x}}$ is the SEM, σ is the SD and N is the number of observations in the sample from which the mean is found.

Non-parametric bootstrap confidence interval

The *bootstrap* is a data resampling methodology for assessing the accuracy of estimates and making inferences about unknown parameters in statistical analysis [60, 61]. The method is based on drawing independent samples from the same data-set from which the target statistic was calculated. It then re-calculates the target statistic on each draw, and the resulting empirical distribution is used as an estimate for the true distribution of the target statistic. Consequently, the method can be used to estimate confidence intervals without making assumptions about the shape of the population distribution. The standard methodology, in contrast, relies on the assumption of normally distributed data, then uses the SD to estimate confidence intervals. However, the distribution of cell viability, which was studied in this project, is truncated, which an assumption of normal distribution would not account for. Moreover, the overall shape and symmetry of the distribution is unknown, making the standard methodology potentially misleading. The non-parametric bootstrap avoids the assumption of normal distribution while being relatively simple to implement.

The procedure for estimating the $(1-\alpha)$ bootstrap confidence interval for a statistic $\hat{\theta}$ is as follows:

1. Generate b boostrap samples by sampling with replacement from the data set from which the target statistic $\hat{\theta}$ was found.
2. For each bootstrap sample, calculate sample the statistic $\hat{\theta}^*$.
3. Estimate the $\frac{\alpha}{2}$ and $1-\frac{\alpha}{2}$ percentiles of the distribution of $\hat{\theta}_i^*$, denoted by $\hat{\theta}^*_{\frac{\alpha}{2}}$ and $\hat{\theta}^*_{1-\frac{\alpha}{2}}$, respectively.
4. A $(1-\alpha)\times 100\%$ bootstrap percentile confidence interval for θ is given by

$$\left[\hat{\theta}^*_{\frac{\alpha}{2}},\quad \hat{\theta}^*_{1-\frac{\alpha}{2}}\right]. \tag{3.4.3}$$

Error propagation

For a function $f(x,y)$, where two independent variables x and y each have an associated uncertainty Δx and Δy, Δf is given by [62]:

$$\Delta f = \sqrt{\left(\frac{\delta f}{\delta x}\Delta x\right)^2 + \left(\frac{\delta f}{\delta y}\Delta y\right)^2} \tag{3.4.4}$$

This is know as Gauss' law of error propagation. For any function on the form

$$f(x,y) = Ax^a y^b, \tag{3.4.5}$$

3.4.4 simplifies to

$$\frac{\Delta f}{f} = \sqrt{\left(a\frac{\Delta x}{x}\right)^2 + \left(b\frac{\Delta y}{y}\right)^2} \tag{3.4.6}$$

Chapter 4

Materials and Methods

4.1 Chlorins

The chlorins investigated in this project were synthesised and supplied by Dr. Katriann Arja at Department of Science and Technology, Linköping University. An overview of chlorins, including chemical formula and properties, are summarised in Table 4.1 and presented in full in Table 1.1. Synthethic schemes and larger images of the chemical structures are included in Appendix A.

Table 4.1: Properties of the chlorins investigated in this project, supplied by Dr. Katriann Arja, Linköping University. The chemical structures of the chlorins are shown in Table 1.1, and included in larger size in Appendix A.

	Attached compound	Chemical formula	Molecular weight [g/mol]
KA20-10.2	Alkynes	$C_{57}H_{42}N_8O_2$	871.02
KA20-11H	Glucose	$C_{73}H_{70}N_{14}O_{14}Zn$	1432.83
KA20-11H-proto	Glucose	$C_{73}H_{70}N_{14}O_{14}$	1367.45
KA20-15H	Galactose	$C_{73}H_{70}N_{14}O_{14}Zn$	1432.83
KA20-15H-proto	Galactose	$C_{73}H_{70}N_{14}O_{14}$	1367.45
KA20-16H	N-acetyl glucosamine	$C_{77}H_{76}N_{16}O_{14}Zn$	1514.93
KA20-16H-proto	N-acetyl glucosamine	$C_{77}H_{76}N_{16}O_{14}$	1449.55

4.2 Optical measurements

Absorption Spectroscopy

To account for any difference in beam intensity of the two paths of light in the spectrometer (see Figure 3.1.1), a baseline measurement was made before finding the absorbance spectrum of the chlorins. This was done by measuring two equal glass cuvettes with the solvent tetrahydrofuran (THF), one as reference and one as sample cuvette. After the baseline measurement was performed, the chlorin was dissolved in THF in the sample cuvette, and measured against the same reference cell. To calculate the molar attenuation coefficient of the compound, the absorbance values were divided by the concentration and path length in accordance with the Beer-Lambert Law (equation 3.1.2) and common procedures for absorption spectroscopy.

Emission Spectroscopy

To measure the emission spectrum, the chlorins were dissolved in ethanol (EtOH) was excited at $\lambda = 422\,\mathrm{nm}$. Emitted photons were collected at a wavelengths from 400 nm to 800 nm. To account for any emission from the solvent and wavelength dependent sensitivity in the detection system, a baseline measurement of solvent only was made with identical excitation wavelength and machine settings. This baseline was found to be very weak, but was anyway subtracted from the final emission spectrum.

Quantum Yield Calculation

In this project, zinc-tetraphorphyrrin (Zn-TPP) was chosen as reference for the investigated molecules, due to its structural and optical similarities to chlorins. First, measurements of sulforhodamine 101 were taken. This compound has a known quantum yield value of 0.95 ± 0.02 [63]. From this, the quantum yield of the reference molecule Zn-TPP was calculated to 0.0278 ± 0.0006 using equation 3.1.7, and Gauss' law of error propagation (equation 3.4.6). The quantum yields of the chlorins were then found using Zn-TPP as reference compound in the same way. It was assumed that the QY of Zn-TPP is independent of excitation wavelength, allowing the value found to be used for measurements at frequencies suitable for the chlorins. To reduce inner-filter and re-absorption effects, the absorbance values of the samples used were kept near or below 0.1. In all QY measurements, EtOH was used as solvent.

Lifetime Measurements

The lifetime measurements of the samples were conducted using Time-Correlated Single-Photon Counting (TCSPC). The principle of the TCSPC technique is the detection of single photons and the measurement of their arrival times in respect to a reference signal, usually the light source. The statistical probability distribution for the emission of these photons is equivalent to the actual intensity versus time distribution for all photons emitted. From this, the exponential decay rate constant, or the *lifetime* of the molecules is found [12].

The chlorins were dissolved in THF and were excited at $\lambda = 403\,\text{nm}$. To avoid multi-photon events, the solutions were diluted until the photon rate from the samples were less than 1 % of the photon rate from the exciting lamp. The experiments were continued until the peak channel reached 5000 counts.

4.3 Cultivation of AY-27 cells

For the cell experiments, the cell line AY-27 was used. This cell line originates from a transitional cell carcinoma in a rat bladder, and was supplied by Professor Steven H. Selman from the Medical College of Ohio, Toledo, USA in 2004. The cells were grown in sterile 75 cm^2 culture flasks, in RPMI-1640 growth medium (Catalogue No. R0883, Sigma Aldrich). The medium was supplemented with 10% fetal bovine serum (FBS) (Catalogue No. F-7524), 0.33% L-glutamine (200 mM, Catalogue No. G-7513), and 1% penicillin/ streptomycin (10 U/mL/10 g/mL. Catalogue No. P-0781). All supplements were obtained from Sigma Aldrich. The cells were kept in a incubator at 37 °C in a humidified atmosphere containing 5 % CO_2.

Twice a week, after reaching 80-90% confluence, the cell cultures were split into new flasks, one with $2 \cdot 10^6$ cells and one with $0.5 \cdot 10^6$. The flasks with the larger initial populations were used for the subsequent sub-culturing, while the others were kept for two weeks as backup in case of infection of the main population. When splitting the cultures, they were first observed in a microscope to visually confirm their health, growth and confluence, to make sure there was no infection or contamination. Then, the medium was removed from the flask, and the cells were washed once in phosphate-buffered saline (PBS) to discard dead cells and traces of old medium. The cells were detached from the flask by adding 3 mL typsin/EDTA solution (0.25%/0.02%, Catalogue No. T-4049, Sigma Aldritch) and incubating at 37 °C for 5 minutes. The trypsinated cells were then transferred to a test tube and centrifuged at 1500 RPM for 5 minutes, causing the formation of a cell pellet in the bottom of the tube. This allowed for the removal of the trypsin/EDTA while leaving the cells. Simultaneous to the centrifuging, a small amount of the suspension was transferred to a Bürker chamber and counted in a microscope, to find the total number of cells in the cell pellet. This process is described in Appendix B. Then, the cell pellet could be resuspended in the tube with an amount of new medium corresponding to a final concentration of 10^6 cells/ml. From this suspension, the two new flasks of $2 \cdot 10^6$ and $0.5 \cdot 10^6$ cells were sown, and medium was added for a total of 15 mL per flask. In addition to the sub-culturing, the cells underwent medium change and washing in PBS once a week.

4.4 Cytotoxicity Assay

The cytotoxicity of chlorins KA20-11H-proto, 15H-proto and 16H-proto (Table 1.1) was measured by alamarBlue cell viability assay. This section presents the experimental design and the different stages of this experiment.

AlamarBlue® cell viability assay

The alamarBlue reagent contains a cell permeable, non-toxic compound called *resazurin* [64]. In its initial state, resazurin is a weakly fluorescent blue indicator dye. In response to cellular metabolic reduction (REDOX), resazurin is reduced to *resosurfin*, which is pink and highly fluorescent. The intensity of the fluorescence is proportional to the number of respiring, *i. e.* living, cells. Due to the light sensitive nature of the reagents, the assay was performed under dark conditions.

Day 1 - Seeding of cells

The cells were trypsinated, centrifuged, and counted by the same procedure as described in section 4.3. Then, cells diluted in growth medium 0.015×10^6 cells/mL were seeded in a 96-well black plate (Costar® Corning Incorporated, Catalogue No. 3603, Sigma Aldrich), with 200 µL (3000 cells) per well. The outermost rows of the plates were left empty to act as reagent-only baselines. The cells were incubated for 24 hours (37 °C, 5 % CO_2).

Day 2 - Incubation with PS

The next day, the medium in the wells was removed, and cells washed once with PBS (150 µL). The PSs was then mixed with new growth medium in 8 different concentrations, ranging from 0.05 µM to 100 µM. For each concentration, 200 µL was added to 8 of the 96 wells in the plate. Of the remaining 32 wells, 16 were refilled with growth medium to act as control group, and the 16 outermost wells were kept empty. From this point on, the wells were kept covered by aluminium foil when not handled, and otherwise kept in minimal lighting. The cells were again incubated for 24 hours.

Day 3 - Removal of PS

To remove the PS, the cells were washed thrice with PBS (150 µL). Fresh medium (200 µL) was added, and the cells were incubated for 24 hours to allow any damage inflicted time to manifest.

Day 4 - AlamarBlue assay

The medium was removed to prepare for the alamarBlue assay. Then, fresh medium with 10 % alamarBlue reagent (Catalog no. DAL1025, Invitrogen) was added to each well. The cells were incubated at 37 °C in darkness for 3 hours. Then, the fluorescence (exitation wavelength 570 nm, emission wavelength 585 nm) of each well was read in a plate reader (SpectraMax i3, Molecular Devices). By plotting the fluorescence emission intensity versus compound concentration, cell viability for each group could then be determined. First, the average value of the reagent only (no cells) wells were subtracted from the average values of all other groups. The average fluorescence intensity measured from the control wells was assigned to correspond to 100 % cell viability. The cell viability for each treated group was then calculated using the formula below.

$$\%\ \text{Cell viability} = \frac{\mathrm{I}_{\text{Treated}}}{\mathrm{I}_{\text{Control}}} \times 100\% \tag{4.4.1}$$

4.5 Photodynamic therapy (PDT)

Investigations were made to determine the photosensitizing effects of selected chlorins (KA20-10.2, -11H, -11H-proto, -15H-proto, -16H-proto) on AY-27 cells. This section presents the experimental design and the different stages of this experiment.

LumiSource® lamp

For the illumination of the AY-27 cells, a LumiSource® lamp from PCI Biotech, Oslo, was used. The lamp is designed specifically for homogeneous illumination of cell dishes, which were placed on top of the lamp and illuminated from below. The light emitted from the lamp is in the range of 400 nm to 550 nm, with a peak at 435 nm. The emission spectrum of the lamp is included in Appendix G. The intensity of the lamp has previously been measured by Prof. M. Lindgren (NTNU, Trondheim, Norway) to 13 mW/cm^2.

Day 1 - Seeding of cells

The cells were trypsinated, centrifuged, and counted by the same procedure as described in section 4.3. Then, cells diluted in growth medium (0.01×10^6 cells/mL) were seeded in 8 × 96-well black plates, with 200 µL (3000 cells) per well. The outermost rows of the plates were left empty to act as reagent-only baselines. The cells were incubated for 24 hours (37 °C, 5 % CO_2).

Day 2 - Incubation with PS

The next day, the medium in the wells was removed, and cells washed once with PBS. PS was then mixed with new growth medium in to the desired concentrations (0 µM to 50 µM. Medium or medium-PS solution (200 µL) was added to each well, according to the experimental setup. An example is shown in Figure 4.5.1. From this point on, the wells were kept covered by aluminium foil when not handled or illuminated, and otherwise kept in minimal lighting. The cells were again incubated for 24 hours.

Day 3 - Illumination

Prior to illumination, the medium containing PS was removed from the dishes, and the cells were washed thrice with PBS (150 µL) to remove any extracellular traces of the PS. Then, PBS (150 µL) was added to cover the cells during the illumination process. Immediately after the removal of the PS and adding of PBS, the cells were placed on the

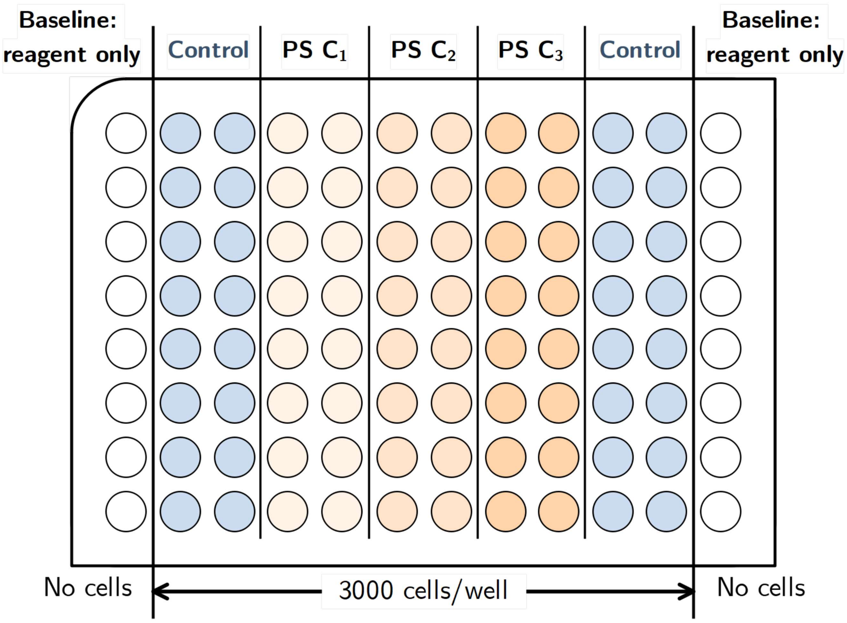
Baseline:
reagent only
Control
PS C1
PS C2
PS C3
Control
Baseline:
reagent only
No cells
3000 cells/well
No cells

Figure 4.5.1: An example of the experimental setup of each plate when investigating the PDT effect of three different concentrations of the same PS.

LumiSource® lamp (435 nm, 13 mW/cm^2) for differing amounts of time, ranging from 10 s to 600 s, as specified by the experimental design. The 0 s groups were not placed on the lamp, but still brought into the room with the other cells to ensure comparable conditions. When removed from the lamp, the dishes were quickly covered to avoid any excess illumination. After exposure to the lamp, the PBS was removed from the dishes and the cells were resupplied with growth medium. The cells were again incubated for 24 hours.

Day 4 - AlamarBlue assay

To determine cell viability after the PDT treatment, an alamarBlue assay was performed for all plates as described in section 4.4.

4.6 Fluorescence microscopy

In this project, the ability of the PSs to enter cells was investigated through fluorescence microscopy, using the excitation and emission wavelengths found from the optical measurements detailed in section 5.2. A Leica TCS SP8 MP confocal laser scanning microscope was used for the analysis. The colocalization of the PSs with various cellular components was also investigated through dyeing of the cell membrane, nucleus, and lysosomes. The properties of the dyes used, bought from Thermo Fisher Scientific, are presented in table 4.2.

Table 4.2: Properties of the dyes used in colocalization analysis of the chlorin PSs. The values for concentration, incubation times, excitation and emission wavelengths were provided by the supplier. All dyes were bought from Thermo Fisher Scientific.

Dye (Catalogue No.)	Structure stained	[C]	Incubation time	Ex. λ	Em. λ
CellMask Green (C37608)	Cell membrane	1 mM	5 min to 10 min	522 nm	535 nm
LysoTracker Blue (L7525)	Lysosomes	50 nM	0.5 h to 2 h	393 nm	420 nm
Draq5 (DR50050)	DNA	10 µM	1 min to 3 min	646 nm	697 nm

Day 1 - Seeding of cells

The cells were trypsinated, centrifuged, and counted by the same procedure as described in section 4.3. Then, cells diluted in growth medium (0.5×10^6 cells/mL) were seeded in 8-well plates (Catalogue No. 80826, Ibidi), with 300 µL (15 000 cells) per well. The wells were situated on top of objective glass, allowing for direct imaging at the end of treatment without needing to remove the cells first. The cells were incubated for 24 hours (37 °C, 5 % CO_2).

Day 2 - Incubation with PS

The next day, the medium in the wells was removed, and cells washed once with PBS. PS was then mixed with new growth medium in the desired concentration. The PS-containing or pure growth medium (300 µL) was added to the wells, according to the experimental setup. From this point on, the wells were kept covered by aluminium foil when not handled, and otherwise kept in minimal lighting. The cells were again incubated for 24 hours.

Day 3 - Staining and imaging

Prior to staining, the medium containing PS was removed from the dishes, and the cells were washed thrice with PBS to remove any extracellular traces of the PS. Suitable staining solutions were prepared according to the specifications of each dye (shown in table 4.2), and was added to the wells according to the experimental design. The cells were then incubated for the amount of time specified for each dye. After incubation, cells were washed two times with PBS and immediately imaged in the confocal microscope.

During imaging, both the dye and PS of each well was illuminated, and their emissions detected in separate channels. In addition to the double-stained wells containing both dye and PS, wells containing only dye, only PS or neither were illuminated with the same wavelengths to check for fluorescence bleed-over in the detection channels. When analysing multiple plates in the same experiment, the other plates were kept in the incubator when not imaged to avoid damage to the cells before analysis.

Colocalization analysis

The methods of simple area analysis and MCC (section 3.3) were performed to find the co-occurrence of the probes tested. These calculations were implemented in a script written in Python 3, in which the threshold could be manually set for each image analysed. This script, along with all images used in the analysis, is included in Appendix C.

Chapter 5

Results

5.1 Overview

An overview of the experiments performed according to the seven chlorins is presented in table 5.1. This section will give a short explanation of the timeline and the thought process behind the experiments.

At the beginning of the project, only KA20-10.2, -11H, -15H and -16H were available for experiments, while the proto-forms of the chlorins were still under synthesis. At this stage, the focus of the experiments was to characterise the basic photophysical properties of these chlorins, and to determine appropriate wavelengths to be used in subsequent fluorescence imaging and PDT experiments. To achieve this, absorption and emission spectra, QY and lifetime measurements were carried out. Then, fluorescence images were taken of the chlorin-incubated AY27 bladder cancer cells. In the first rounds of imaging, the plasma membranes of the cells were stained, to confirm the uptake of the compounds into the cells. From these images, additional dyes of interest were identified and imaged in later rounds. From the results gained from this first phase of the project, the Zn-forms of the chlorins were observed to exhibit nearly identical optical properties. Due to the limited time available, it was not possible to continue running all experiments on all chlorins, and KA20-11H was chosen to act as a representative for the Zn-forms for the following PDT experiments. In the first round of the PDT cell survival assays, several concentrations of KA20-10.2 and KA20-11H were tested, as the potency of the chlorins as PSs in PDT was unknown.

At this point, the proto-forms of the chlorins were ready, and the plan was to repeat

Table 5.1: Overview of experiments performed for each chlorin. PDT refers to blue-light illumination.

Chlorin	Optical measurements	Fluorescence microscopy	Cell experiments
KA20-10.2	Absorbance/ emission spectra Quantum yield Lifetime Singlet oxygen yield*	With labelled · Cell membrane · Lysosomes	AlamarBlue assay (PDT): · 1 µM · 5 µM · 10 µM · 50 µM
KA20-11H	Absorbance/ emission spectra Quantum yield Lifetime Singlet oxygen yield*	With labelled · Cell membrane · Nucleus	AlamarBlue assay (PDT): · 1 µM · 5 µM · 10 µM · 30 µM
KA20-11H-proto	Absorbance/ emission spectra* Lifetime* Singlet oxygen yield*	Not performed	Dark toxicity AlamarBlue assay (PDT): · 1 µM · 5 µM · 10 µM
KA20-15H	Absorbance/ emission spectra Quantum yield Lifetime	With labelled · Cell membrane · Nucleus	Not performed

Continued on next page

* Experiments performed by Prof. M. Lindgren, Department of Physics, NTNU.

Table 5.1 – continued from previous page

Chlorin	Optical measurements	Fluorescence microscopy	Cell experiments
KA20-15H-proto	Absorbance/ emission spectra* Lifetime* Singlet oxygen yield*	Not performed	Dark toxicity AlamarBlue assay (PDT): · 1 µM
KA20-16H	Absorbance/ emission spectra Quantum yield Lifetime	With labelled · Cell membrane · Nucleus	Not performed
KA20-16H-proto	Absorbance/ emission spectra* Lifetime* Singlet oxygen yield*	Not performed	Dark toxicity AlamarBlue assay (PDT): · 1 µM

* Experiments performed by Prof. M. Lindgren, Department of Physics, NTNU.

the basic photophysical measurements and fluorescence imaging for these, as well, to gain a good foundation for comparison with the earlier chlorins. However, due to the COVID-19 outbreak, lab access became limited, and would remain so for the rest of the project period. Because of this, it was decided that the author should concentrate her efforts in the cell lab, while supplementary optical measurements were performed by Prof. M. Lindgren (Department of Physics, NTNU). Some of the supplementary measurements, noted (*) in table 5.1, are included in Appendix E.

During the first round of PDT experiments, 5 µM was found to be a suitable concentration of KA20-11H-based PDT. In subsequent experiments, PDT with KA20-11H-proto was tested for this concentration. However, as the proto-forms were new, and their behaviour relative to the Zn-forms not known, supplementary concentrations (1 µM, 10 µM) were included. As the proto-form was found to be more effective than its Zn-form counterpart, the later experiments with KA20-11H-proto, -15H-proto and -16H-proto were performed at 1 µM, instead.

5.2 Optical measurements

Absorption and emission

The molar attenuation coefficients of KA20-10.2, 11H and 11H-proto as a function of incident wavelength are presented in Figure 5.2.1. The real and normalised emission as a function of wavelength are presented in Figure 5.2.2. The spectra of 15H and 16H were also measured, and found to be identical to those of 11H. Likewise, the spectra of 5H-proto and 16H-proto were found to be identical to that of 11H-proto. All optical measurements of the proto-versions of the chlorins were provided by Prof. M. Lindgren, NTNU, and included in the master's thesis for comparison. The λ_{max}-values for the chlorins are presented in table 5.2.

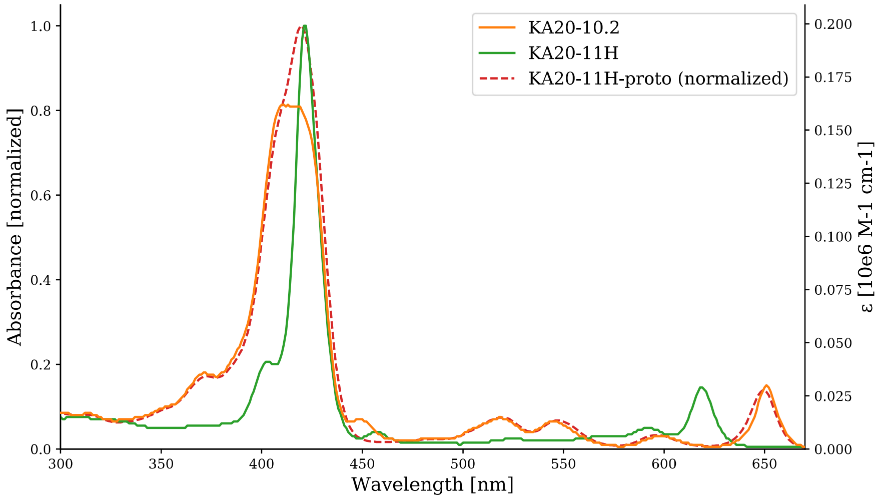

Figure 5.2.1: Molar attenuation coefficients ϵ of 10.2, 11H and 11H-proto in THF solution. Not shown are the ϵ of 15H and 16H, or 15H-proto and 16H-proto, which were identical to 11H and 11H-proto, respectively. The measurements of 11H-proto were provided by Prof. M. Lindgren, NTNU.

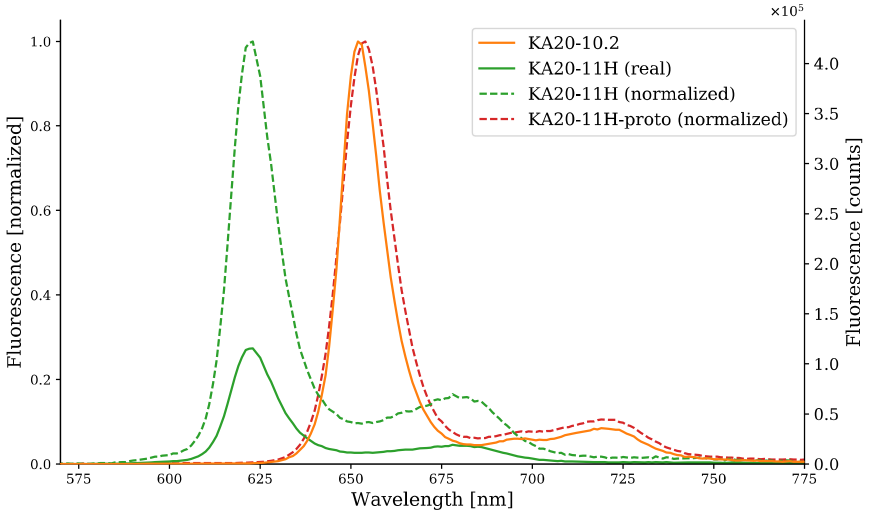

Figure 5.2.2: Real and normalized emission spectra of 10.2, 11H and 11H-proto in EtOH solution, excited at $\lambda = 422\,\text{nm}$. A baseline measurement of EtOH emission was subtracted from the fluorescence values. Not shown are the spectra of 15H and 16H, or 15H-proto and 16H-proto, which were identical to 11H and 11H-proto, respectively. The measurements of 11H-proto were provided by Prof. M. Lindgren, NTNU.

Quantum Yield

The measurements of fluorescence used to calculate the QY of the chlorins are shown in Figure 5.2.3, and the resulting values found are presented in Table 5.2. KA20-10.2 was found to have the highest QY value at 19.1 %, while the glycosylated chlorins had reduced QYs of around 5 % to 6 %.

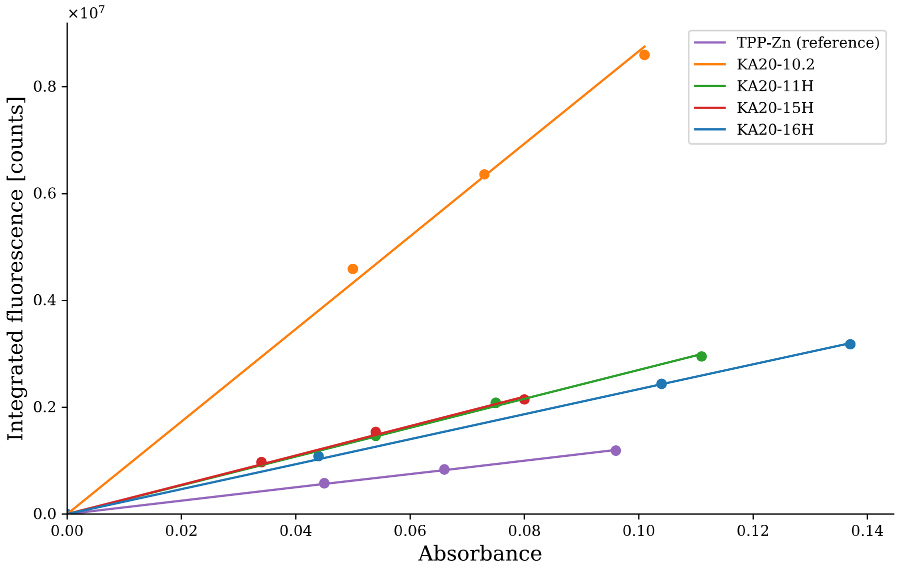

Figure 5.2.3: Linear regression applied to measurements of integrated fluorescence of different concentrations of KA20-16H, KA20-15H, KA20-11H and KA20-10.2. Also included is the reference measurements of TPP-Zn, with known QY of 2.8 %. The samples were excited at a wavelength of 422 nm, and EtOH was used as solvent for both chlorins and reference. A baseline measurement of the fluorescence of the solvent at 422 nm was subtracted from the values of the fluorescence of the chlorins and reference.

Lifetime Measurements

The experimental decay intensity spectrum for KA20-16H and KA20.10.2 is shown in Figure 5.2.4, together with the single-exponential fit. Similar spectra were found for the other chlorins as well. In table 5.2, the resulting τ values are presented. For chlorins KA20-11H, 15H and 16H, the lifetimes were found to be close to 1.5 ns, while KA20-10.2 displayed a lifetime of more than 10 ns.

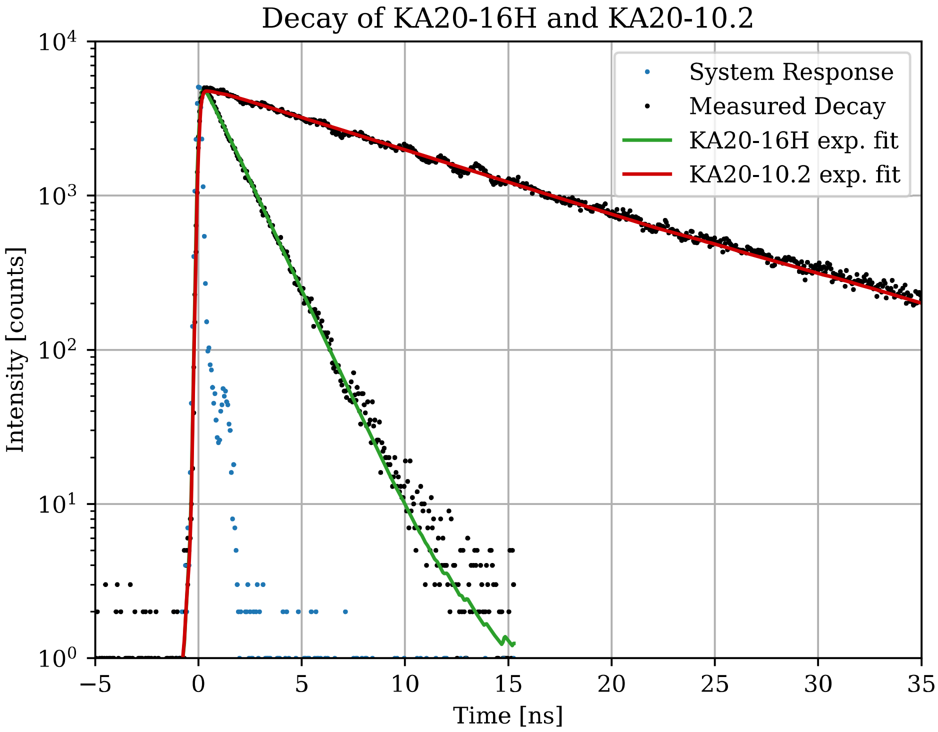

Figure 5.2.4: Intensity of decay as a function of time for KA20-16H and KA20-10.2, after excitation at $\lambda = 403\,\text{nm}$. Emission was measured at 625 nm for KA20-16H and 650 nm for KA20-10.2. Both decay curves are single-exponential fits. Not included are the measurements of KA20-11H and KA20-15H, which were very similar to KA20-16H.

Table 5.2: Summary of results from spectroscopy measurements of the chlorin PSs.

	Absorption maximum [nm]*	Emission maximum [nm]*	Quantum Yield**	Lifetime [ns]**
KA20-10.2	412	652	0.191 ± 0.005	10.30 ± 0.03
KA20-11H	422	622	0.060 ± 0.001	1.503 ± 0.004
KA20-15H	422	622	0.061 ± 0.001	1.495 ± 0.004
KA20-16H	422	622	0.052 ± 0.001	1.508 ± 0.004

*± 1 nm.

** error estimation is based on the root mean squared error of the regressional fit, given uncertainties of table values and Gauss' law of error propagation.

5.3 Fluorescence imaging

Fluorescence images were taken of cells incubated with KA20-10.2, KA20-11H, KA20-15H and KA20-16H, and stained with various dyes (table 4.2). Of these, KA20-10.2 had the largest fluorescence yields, and was the easiest to capture in the microscope. Example images of KA20-10.2 fluorescence with stained cell membranes or lysosomes are presented in figure 5.3.1. Several images from each group were analysed to find the co-occurrence between the two, presented in table 5.3. All images analysed are included in appendix C.

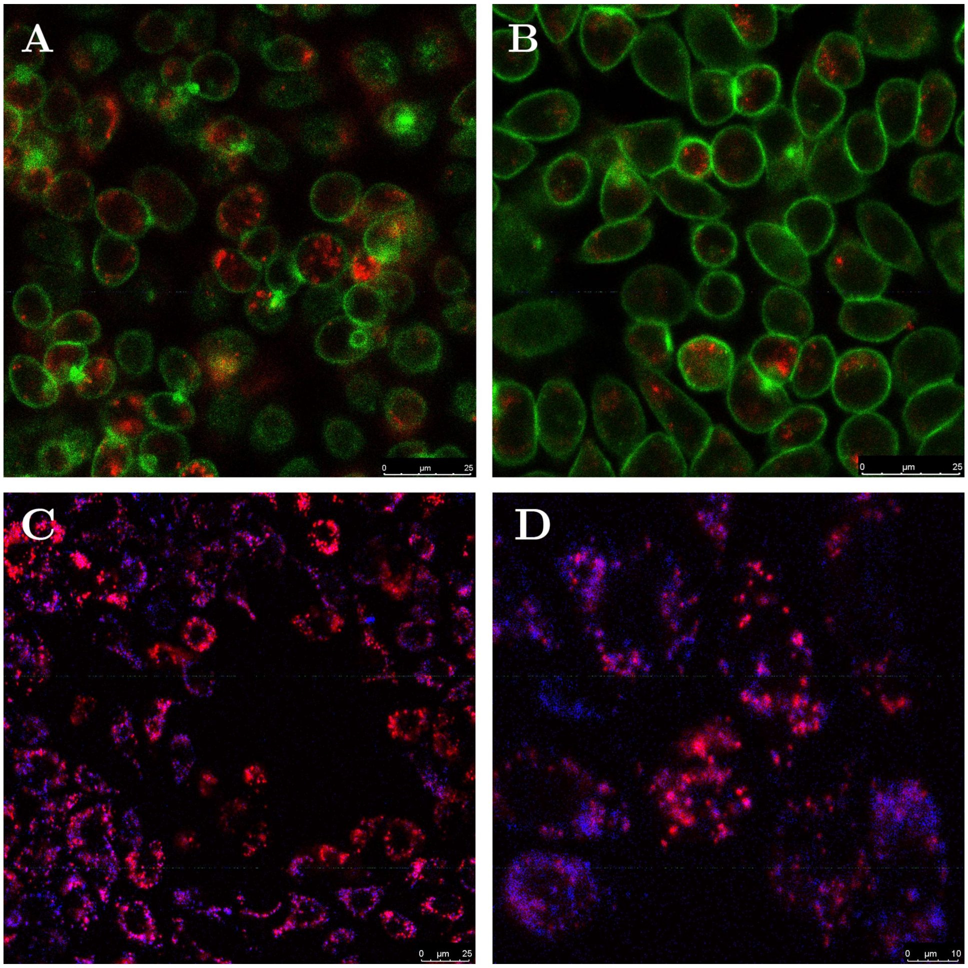

Figure 5.3.1: Fluorescence images showing AY27 cancer cells, incubated with 1 µM KA20-10.2 (red channel). A) and B): Cells stained with CellMask Green (green channel), which marks the cell membrane. C) and D): Cells stained with LysoTracker Blue (blue channel), which marks lysosomes. Images were taken in a CLSM microscope.

While KA20-10.2 was easily imaged in the fluorescence microscope, KA20-11H, -15H and -16H turned out to be more challenging. Most attempts at imaging the fluorescence of these compounds proved unsuccessful, with the exception of a group of cells also stained with Draq5, which targets the nuclei and DNA of cells. Images from this group are presented in figure 5.3.2.

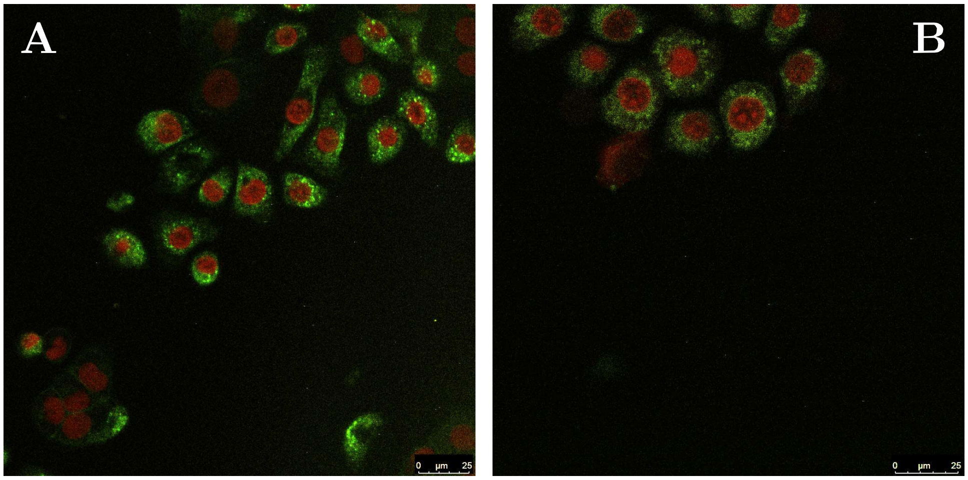

Figure 5.3.2: Images showing the fluorescence of A) KA20-11H and B) KA20-16H (green channel) in AY27 cancer cells, taken in a CLSM microscope. Cells in both images were incubated with 10 μM of the chlorin compound. The nuclei of the cells were stained with Draq5 (red channel).

For the colocalization analysis, finding if there was any co-occurrence of the chlorins and the organelles was of greatest interest at this point. Therefore, determining coefficients indicating co-occurrence were prioritised over intensity correlation coefficients. First, the highest-quality images were chosen, and simple area analysis was performed as described in section 3.3. The overlap percentage of the channels was calculated from equation 3.3.1. Simple area analysis has the advantage of being intuitive and easy to implement, however, information on the intensity distributions of the fluorescence is lost when using this method. To address this, Mander's correlation coefficients M1 and M2 were found, as well. Here, more weight is given to areas of greater signal intensity, but the resulting coefficients are harder to interpret. These coefficients and their differences are explored more in-depth in section 3.3. For both methods, the thresholds were set manually. The results from the analysis are presented in table 5.3. The script written to perform the calculations for both methods is included in Appendix C.

Chlorin	Stain	C_f (%)	M1	M2	N
KA20-10.2	LysoTracker Blue	24.6 ± 6.7	0.33 ± 0.14	0.45 ± 0.05	5
KA20-10.2	CellMask Green	4.8 ± 2.8	0.24 ± 0.11	0.06 ± 0.03	4
KA20-11H	Draq5	9.8 ± 0.3	0.38 ± 0	0.28 ± 0.01	2
KA20-16H	Draq5	10	0.18	0.29	1

Table 5.3: Resulting values from colocalization analysis of cells incubated with chlorin PSs in combination with stains. C_f is the overlap percentage, found from simple area analysis. M1 and M2 are Mander's correlation coefficients, where the PS is set as channel 1, and N shows the number of images analysed. The standard deviation of the values is given where $N > 1$. All thresholds were set manually.

5.4 PDT experiments

The results from the PDT cell survival assays (alamarBlue) of KA20-10.2, KA20-11H and KA20-11H-proto (5 µM) are presented in Figure 5.4.1. The results from PDT assays of the proto-forms of the chlorins (KA20-11H-proto, -15H-proto, 16H-proto, 1 µM) are presented in Figure 5.4.2. The results for KA20-10.2 are based on two biological replicates, while the results for all other chlorins are based on three biological replicates. The values for the control group (light only) are the mean values of controls from all experiments shown in each plot. To find the cell survival ratio, the values for each compound were divided by the mean control value (no light, no PS) for that experiment. For each value, a baseline measurement of the fluorescence from the reagent only (no cells) was subtracted.

The 95 % confidence interval was found by non-parametric bootstrapping analysis, as described in section 3.4. For each data point, all relative survival values from all experiments were collected. From this sample, 1000 new samples of the same size were drawn, and the confidence interval was found from the distribution of the mean values of these samples. This process was repeated for every time point of each group.

In addition to the results shown in Figure 5.4.1 and 5.4.2, additional measurements were made of KA20-10.2 (1 µM, 10 µM, 50 µM), KA20-11H (10 µM, 30 µM) and KA20-11H-proto (10 µM). These results are included in appendix D. Measurements were also made for longer illumination times than what is included in the figures: 240 s for KA20-10.2, where the cell survival was measured at 40 %, and 600 s for all other compounds and light only groups, which all measured at less than 5 % and around 100 %, respectively.

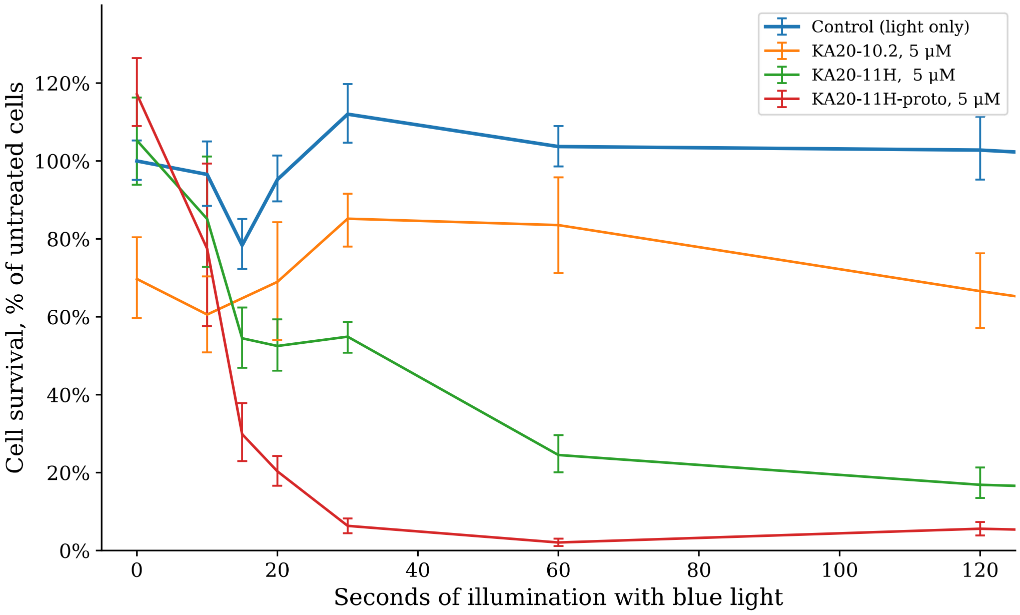

Figure 5.4.1: The relative cell survival of AY27 cells after treatment with PS and blue light (435 nm), or light only, compared to untreated cells. The error bars show the 95 % confidence interval of the mean values.

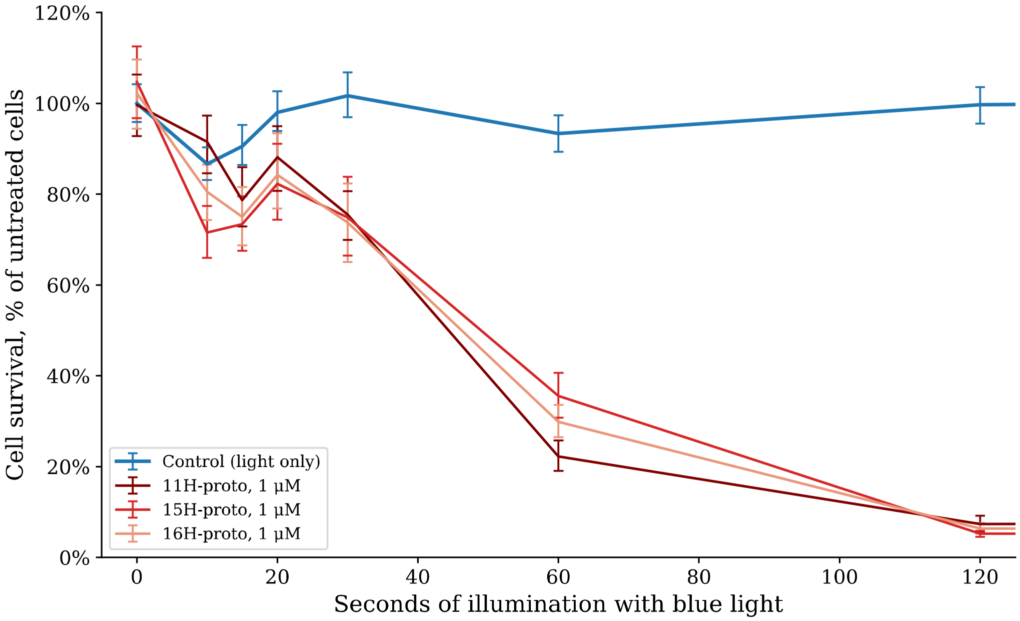

Figure 5.4.2: The relative cell survival of AY27 cells after treatment with PS and blue light (435 nm), or light only, compared to untreated cells. The error bars show the 95 % confidence interval of the mean values.

Chapter 6

Discussion

This project aimed to study the potential of the KA20 family of chlorins as photosensitizers (PSs) in photodynamic therapy (PDT), and arose as a collaboration between Department of Physics, NTNU, and Department of Physics, Chemistry and Biology, Linköping University, where the chlorins were synthesised. There were 7 novel chlorins in this family to investigate (as outlined in Table 1.1). Due to time limitations, this work focused on the essential properties for PDT applications: Basic photo-physical properties, intracellular uptake and distribution, and effects on cell viability when used as PS in PDT on rat bladder cancer cells (AY-27). Suggestions for further study are summarised in section 6.3.

6.1 Discussion of the results

Basic photophysical properties of the PSs

The absorbance and emission of the chlorins, listed in Table 1.1, are presented in Figure 5.2.1 and 5.2.2. The spectra show features common to chlorin-based molecules, as discussed in *e.g.* Zhu *et al.*, 2018 and Pereira *et al.*, 2018 [65, 66]. The absorbance spectra show a global maximum for blue light, around 420 nm, and a local maximum for longer-wavelength red light, at around 650 nm. The emission maximum appears at 652 nm. With the introduction of a zinc atom in the chlorin ring (KA20-11H, -15H and -16H), both the lowest-energy wavelength absorption maximum and the emission spectra were shifted towards shorter wavelengths, to around 620 nm and

625 nm, respectively. Quantum yield (QY) measurements of KA20-10.2 and the Zn-form glycoconjugates showed that fluorescence emission was substantially reduced by the introduction of the sugar groups, from 19.1 % to around 6 %. Lifetime measurements showed a corresponding reduction in fluorescence lifetime, as well, from 10.3 ns to around 1.5 ns.

Due to time constraints, the spectra for the proto-form was not measured for the same concentrations as the previous chlorins, and the QY values were not determined. Therefore, any differences in the magnitude of the absorbance or fluorescence cannot be stated with certainty. However, measurements made of singlet oxygen yield by Prof. M. Lindgren, included in Appendix E, showed similar values for both the Zn- and the proto-forms. In addition, cell survival assays proved the proto-forms to be effective at killing cells in blue-light PDT, indicating significant reactive oxygen species (ROS) production. In light of this, it seems likely that the proto-forms would exhibit a reduction in fluorescence yield compared to KA20-10.2, like the Zn-forms, but quantum yield measurements of the proto-forms should be performed to confirm this.

Fluorescence microscopy and colocalization analysis

The chlorin KA20-10.2 has a relatively large quantum yield and was easily imaged in the fluorescence microscope. When staining the cell membrane, signal from the compound was observed at various spots inside the cells to a large degree, confirming that AY27 cells exhibit uptake of the chlorin. However, interestingly, it was observed that the signal from the chlorin would vary between regions. Some regions, such as Figure 5.3.1 A), presented relatively large amounts of fluorescence in nearly every cell, while for others, as shown in Figure 5.3.1 B), mostly empty cells and only a small amount of scattered fluorescence were observed. This could be caused by poor solubility of the chlorin in the medium, causing uneven concentrations across the cell layer. Moreover, the fluorescence was not distributed evenly throughout the cells, but seemed to accumulate into high-signal clusters. This could indicate that the chlorin does not diffuse freely in the cytoplasma. Instead, it may be contained in lysosomes, or it may exhibit a preference for a specific organelle.

To shed some light on this, images were also taken of cells with stained lysosomes with LysoTracker Blue. Visually, the signals from the lysosome dye and the chlorin seemed to have some correlation. As outlined in section 3.3, there are ways to quantify the localisation of a fluorophore by comparison to dyes which are known to localise within specific cell compartments. In this project, two such methods were utilised:

Simple area analysis and Mander's correlation coefficients (MCC). Simple area analysis was chosen due to its simplicity and intuitiveness, providing a quick and easy way to quantify the correlation of two probes. Then, to provide more information on the influence of intensity difference, MCC was determined for the same images. Simple area analysis of the two channels gave a mean overlap percentage of 24.6 %. Meanwhile, a mean value of 4.8 % was determined for the cell membrane/KA20-10.2 overlap. This indicates that co-localization of the chlorin with the cell membrane is very limited, perhaps even anti-correlated. For the lysosomes, the value is significantly higher. While it is not large enough to draw any conclusion about co-localization, anti-correlation between the two can be ruled out. Thus, it can be confirmed that some of the chlorin fluorescence coincides with the lysosomes. When looking at the MCC M1 and M2, where the intensity in the overlapping areas is taken into account, the colocalization value increases further. Nearly half of the signal intensity from the lysosomes originates from areas where KA20-10.2 signal is present, implying that nearly half of the lysosomes contain some amount of the chlorin. Meanwhile, about one third of chlorin fluorescence originates from areas also containing lysosome fluorescence, implying that approximately 30 % of the PS absorbed by the cells are trapped in lysosomes. However, these results are vulnerable to error, due to the thresholds for the analysis being set manually. This is discussed further in section 6.2.

Fluorescence images of the Zn-forms of the chlorins (KA20-11H, -15H, 16H, Table 1.1) were also performed. This was associated with much greater difficulty, as the fluorescence yields of the Zn-forms are significantly reduced compared to KA20-10.2, as indicated by the lower QY values (Table 5.2). However, after increasing the concentration from 1 μM to 10 μM, signals from the Zn-forms could be captured. These images did not show the uneven uptake present in the KA20-10.2 images, as all cells seemed to show equal amounts of signal, evenly distributed within the cytoplasma. The introduction of sugar groups seems to have facilitated increased uptake in the cells. Additionally, confinement to lysosomes seem unlikely, as the signal was not clustered but spread across the cytoplasma. Colocalization analysis also showed low, but present, overlap with the nucleus stain, indicating that a small amount of the PS sat on the nuclear membrane or had leaked into the nucleus itself. Overall, the addition of sugar groups in KA20-11H, -15H and 16H seem to increase the solubility, uptake and cellular distribution of the chlorins, resulting in increased potential as PSs. This is also in line with the initial intentions of the study, and was previously observed by Arja *et al.* for similarly labelled porphyrins [67], although more details and comparisons between different sugar moieties should be carried out. However, it must be kept in mind that the increased concentrations used in the imaging process may not give representative results for the lower concentrations used in the actual PDT treatment on AY27 cells.

Cell viability after blue-light PDT treatment

PDT experiments were initially done on AY27 cells incubated with different concentrations of KA20-10.2 (1 µM to 50 µM) and KA20-11H (1 µM to 30 µM) (Figure 5.4.1). AlamarBlue cell viability assays showed a strong PDT effect for KA20-11H. For 5 µM, the viability of the treated cells dropped to 50 % of the untreated cells after about 40 s, and to less than 20 % after 120 s. The illumination point at 240 s, not included in Figure 5.4.1, showed less than 10 % survival. In other words, the illumination of the treated cells had a strong effect on their viability for this compound, indicating that a photodynamic effect is present.

In contrast, for the viability of cells incubated with KA20-10.2, a comparable dependency on light exposure was not present. For illumination times of 0 s to 120 s, the cell survival stayed between 60 % to 80 %, and only dropped further to 40 % after 2 min of light exposure. Additionally, viability of cells exposed to only the compound without light was only 70 %. This indicates that much of the damage seen is due to dark toxicity, and not a photodynamic effect. This trend held true for the other concentrations of KA20-10.2 tested, as well (Appendix D, Figure D.1).

The differences between the two chlorins corroborates findings from the previous photophysical results. As KA20-10.2 was found to have a significantly higher fluorescence quantum yield than the glycosylated KA20-11H, its potential for singlet oxygen production is correspondingly lower. As explained in section 2.2, while other ROS from other pathways exist, $^1O_2$ accounts for most of the damage to cells in PDT. In addition, as discussed in the previous section, the fluorescence images taken of KA20-10.2-incubated cells showed only varying uptake, and indicated some overlap with lysosomes. From this, it seems like the glycosylation of the chlorin helps its PDT potential in the following ways: it increases its uptake in cells, improves its distribution into the cytoplasma, and increases its ROS production. All of this together elevates the chlorin from having nearly no photodynamic properties to being an effective PS. In addition to this, the viability results imply that the addition of sugar groups actually decreases dark toxicity, as well, though the mechanism behind this change is not known. Regardless of the reason, a low dark toxicity is crucial in a PS meant for PDT, as this is part of what shields healthy cells from damage.

In Figure 5.4.1, results from the experiments with KA20-10.2 and KA20-11H discussed above are shown with results from PDT experimens with KA20-11H-proto of the same concentration. Here, it is shown that the removal of the zinc atom from the chlorin ring increases the effectiveness of the treatment even further. There could be several reasons for this. For example, increased absorption of the incident wavelengths or a larger overlap with the lamp emission spectrum could increase photodynamic effect for the same illumination times. While the absorption spectrum for the proto-form does not differ much from the Zn-form, they are not identical, which could mean that one had a more favourable absorption of the incident wavelengths than the other. To investigate this, measurements were made of the LumiSource lamp spectrum (Appendix G), which showed the overlap percentages of area-normalised spectra to be very similar for KA20-11H and KA20-11H-proto (8.1 % vs 7.4 %). However, the spectra of the proto-forms were not taken at the same concentrations as the other chlorins, meaning that their magnitude compared to the Zn-form is not known. An overall higher optical density could lead to increased photosensitizing activity, despite the similar overlap values of the chlorins with the lamp. A decreased fluorescence quantum yield could also lead to an increase in the ROS production, and thus greater photodynamic effect, if the singlet oxygen yield increases correspondingly. However, singlet oxygen yield measurements supplied by Prof. M. Lindgren showed no significant difference between the Zn- and proto-forms of the chlorins, suggesting that it is not a greater $^1O_2$-generation efficiency that causes the increased PDT-effect for the proto-forms.

Another possibility could be increased cellular uptake of the proto-forms relative to the Zn-forms, or alternatively a more preferable intracellular distribution. It is well known that the singlet oxygen lifetime (and thus diffusion length) is strongly depending on solvent polarity. For example, the lifetime is around 1 μs in water [68], but more than 200 μs in CHCl3, as documented by measurements performed by Prof. M. Lindgren, included in Appendix E. PSs in more hydrophobic regions thus has longer time available to react and damage a biomolecule. Thus, if the proto-form chlorin absorbed by the cell targeted such vulnerable regions to a greater degree, this could lead to increased cell death from PDT even if the chlorin had the same production of $^1O_2$ as the Zn-form. That said, no fluorescence microscopy or any quantitative measurement of cell uptake or distribution was performed for the proto-forms, as informed in Table 5.1, so the true mechanism behind the increased effects will have to await further studies.

As optical measurements of the chlorins showed that proto-forms were more or less optically identical, any difference in PDT effects between the three were likely to be caused by cellular response to their sugar groups. Finding out if any particular sugar had a better effect was the motivation behind comparing viability assays for

KA20-11H-proto, KA20-15H-proto and KA20-16H-proto in PDT, for which the results are presented in Figure 5.4.2. As expected, the viability curves for these chlorins were very similar. That said, some small statistically significant differences between the glucose and galactose-glyconjugates (11H-proto and 15H-proto) were found from the measurements. Compared to galactose, glucose made the chlorin less PDT effective after 10 s of illumination, but more effective after 1 min. This difference may be caused by variations in cellular uptake and distribution for the two sugars. However, the observed difference only amounts to a few (less than 5) percentage points, at two of eight data points. This could also be explained by natural variation skewing the results, as the confidence interval accuracy follows the quality of the input data. To confirm any cell preference for one sugar group or the other, the difference should be confirmed by repeated experiments.

Increased PDT effects post short illumination times

Looking at the plots of the cell viability assays (Figures 5.4.1, 5.4.2, Appendix D), an interesting observation can be made. For nearly all groups, including the control groups, a sharp drop in cell viability is seen for low illumination times, immediately followed by a recovery. For treated groups, the viability then drops further, while the control groups stay near 100 % for the longer illumination times (30 s to 120 s), including measurements after 600 s (not included in the results). While the magnitude of the drop varied, this phenomenon was clearly seen for all the experiments run during the project, the only exceptions being the steepest survival curves.

This effect is also seen in conventional radiotherapy, where cancer cells treated with radiation doses lower than 0.3 Gy have a lower survival rate than higher doses [69][70], as illustrated in Figure 6.1.1. This is known as the hyper-radiosensitivity (HRS)/increased radioresistance (IRR)-transition. The generally accepted explanation is that some threshold of damage amount must be met to induce the repair processes in the cells. As explored in section 2.3, the cells will initiate repair mechanisms in response to deoxyribonucleic acid (DNA) damage. This damage is detected at various checkpoints in the cell cycle, and the cell is arrested at the checkpoint until the damage is repaired. This stops a damaged cell from attempting mitosis and dying in the process. Evidence suggests that the metabolic cascade which initiates the G2/S-phase checkpoint (described in section 2.3), in particular, is not triggered for low radiation doses. This causes non-viable cells to proceed to DNA synthesis. If the dose is increased, the checkpoint is triggered, and the same cells will be repaired before proceeding.

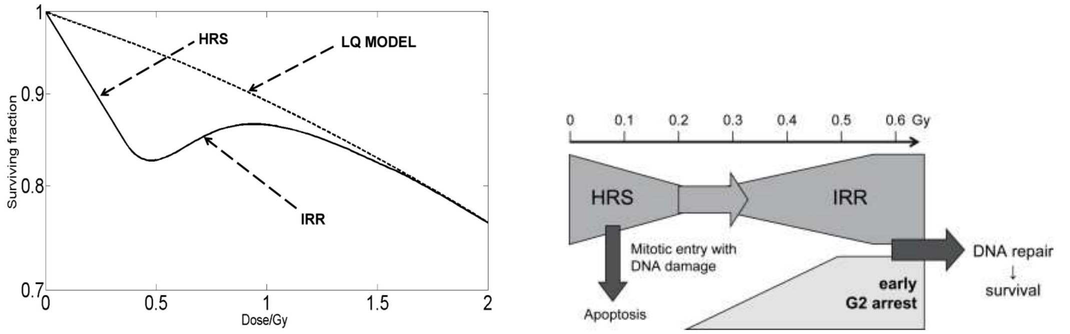

(a) Surviving fraction of cells as a function of dose according to linear quadratic model (1) (dashed line) and with the HRS/IRR phenomenon (solid line). [71]

(b) Current understanding of the processes regulating the HRS/IRR transition. [70]

Figure 6.1.1: Illustrations of the HRS/IRR-transition, as it is observed in conventional radiotherapy.

While PDT and conventional radiotherapy are not equivalent, they work based on many of the same principles. The end goal of both is to cause damage to DNA or other critical organelles, and they both utilise ROS generation to do so [72]. It is therefore not surprising that the HRS/IRR-transition known in radiation therapy shows up in PDT. It seems likely that, if more measurements were made for illumination times shorter than 10 s, the effect would have been found for the steeper curves, as well. An interesting observation is that this effect is also found in the light only control groups. This implies that light from the lamp alone is enough to both cause up to 20 % cell death in the HRS region, and to trigger the repair pathways of the IRR region. However, after this, control groups stayed at around 100 % viability for all longer illumination times, up until the last measurements made at 10 min of blue light exposure. This shows that once the repair pathways are initiated, the light alone cannot induce enough damage to overwhelm them, the way the presence of a PS does - at least not within the parameters tested in this project.

The KA20 family of chlorins as PSs in PDT

The experiments carried out in this thesis show several properties suitable for PDT by the KA20 family of chlorins. Cellular uptake and PDT effects on cells of the PSs have been confirmed by fluorescence microscopy and cell survival assays. The photo-physical properties of the chlorins are promising, as well. As explained in section 2.2, a high absorbance of red/infrared light is important, as higher-energy photons do not penetrate tissue sufficiently. The area between 600 nm to 800 nm is generally regarded as the effective region of PDT, and one of the currently most frequently used PS Photofrin® activates at 630 nm [5]. With strong absorption maxima at 650 nm, the chlorins studied in this project can be excited at suitable wavelengths for PDT.

However, one of the weaknesses of the first-generation PS Photofrin® is the fact that its absorbance is much greater for blue light than for red light. This causes the PS to also be activated by other light sources to a large degree. The fact that the investigated chlorins show a clear peak in the red light region at all is an improvement on the very weak absorption bands of Photofrin®, but this could be a challenge for these chlorins as well, as their absorbance maximum at around 420 nm is of much greater magnitude than the local maximum in the red light region.

That said, the spectra found for the KA20 family are partly similar to chlorin derivatives such as Chlorin e6 (Ce6) [73] than the porphyrrin derivative active in Photofrin®. Some second-generation PSs based on Ce6 have been approved, and other are under development. Reports on these indicate increased selectivity, phototoxicity and clearance in patients, resulting in mild photosensitivity for only up to one week [9, 74]. It seems likely that the chlorins tested in this project would show similar results, due to the large similarities in both optical properties and structures. If so, they would greatly improve the side effects caused by Photofrin, despite of their large absorbance of blue light.

Another interesting observation is that the fluorescence of the compounds decrease greatly in magnitude with the introduction of sugar groups in KA20-11H, 15H and 16H, compared to KA20-10.2. As discussed earlier in this chapter, the proto-forms are expected to exhibit a similar decrease, as seen from Figure 2.1.1 and 2.2.1, with fluorescence and ROS production as competing processes. Therefore, a high quantum yield of fluorescence is directly detrimental to the effectiveness of a PS.

Lastly, preliminary cytotoxicity assays were performed for KA20-11H-proto and KA20-16H-proto, the results of which are included in appendix D. As only a single assay was performed, and relatively large variations within the groups were observed, this experiment should be repeated for greater accuracy. However, it is implied by the results that the dark cytotoxicity for PDT-relevant concentrations is low, as the viability for 1 μM for both compounds was well above 90 %. A low dark toxicity is crucial for an effective PS, and these preliminary results are promising in this regard.

6.2 Evaluation of procedures

Experiments conducted on living organisms, lasting several days, will always be associated with uncertainties due to the numerous factors which may influence the outcome. The cells' environment and treatment throughout *in vitro* experiments cannot be kept exactly identical, and small differences will occur both from one experiment to the next and between populations of the same experiment. The condition of the cells may vary from one day to the next, and abnormalities may not be caught by visual inspection, particularly if the inspector has limited previous experience in cell laboratory work, as is the case for the author. Contamination by foreign, harmful entities such as bacteria, virus or fungi is also always a concern when working with cell cultures, but such infections were luckily not observed during this project.

Consequently, several steps must be taken to minimise these uncertainties and produce reliable results. In this project, the same set procedure (alamarBlue) was followed as closely as possible for the experiments to make sure that the outcomes could be compared. By verifying the condition of cells from different dishes in a microscope at various points throughout the experiments, the chance of detecting any contamination of the cells was increased. And, in order to ensure as similar conditions as possible for the populations, all cells were given the same treatment and kept together whenever possible. Lastly, the most important measure to ensure reliable results is to repeat the same experiment multiple times, and to include many parallels in each repetition. Therefore, with a few exceptions due to time constraints, three biological replicates of the experiments were performed. These are measurements repeated in the same way for biologically distinct samples, meaning they are performed on cells seeded in separate instances. This is intended to limit the influence of random biological variation on the results.

While the above precautions help in limiting the uncertainties associated with cell experiments, some potential sources of errors or inaccuracies were present during the experiments. These are discussed below.

Colocalization analysis

As touched upon in earlier sections, KA20-10.2 was easily imaged in the fluorescence microscope, while the reduced fluorescence yields for the Zn-forms of the chlorins caused some difficulties in this regard. While several rounds of images were taken, most showed only very low signal which required substantial amplification to be seen clearly. When signal is amplified, noise is, as well, potentially leading to images of poor quality with a low signal-to-noise ratio (SNR). As discussed in section 3.3, such images are poorly suited for colocalization analysis, as noise will significantly influence the results. Choosing suitable thresholds and regions of interest can mitigate this, but in the end, the quality of the analysis can only be as good as the quality of the input image. Of the images taken of KA20-11H, KA20-15H and KA20-16H, only three were deemed to be of good enough quality to perform colocalization analysis, and the signal in these had to be amplified to a significant degree, as well. Thus, the quality of the analysis is affected both by the relatively poor quality of the images, and the fact that only one or two images were analysed in each group.

In addition, the thresholds used in the analysis were set manually. As explained in section 3.3, the thresholds set can have a large impact on the outcome of the analysis. When set manually, they make the methods vulnerable to user bias, and make the results less reliable. Ideally, unbiased methods for threshold determination such as Costes' method should be implemented to avoid this subjectivity in the results.

The alamarBlue assay

The cell viability assay used in this project was not known to the cell lab at Department of Physics before the chlorin studies. Introducing new protocols in this manner is always associated with some risk of error, as the best practises and any pitfalls of a method often are learned by experience. With the assay being new to the supervisors, as well, the probability of identifying any recurring mistakes made during the procedures was lessened. The accuracy of the assay for measuring cell viability was also an unknown.

While lack of experience cannot be entirely mitigated, the accuracy and dependability of the new protocol can be investigated with comparison to a known method. In this case, cell viability had previously been measured by MTT assays [75] at Department of Physics for the AY27 cell line. To confirm alamarBlue's accuracy, an additional assay was carried out for a boron dipyrromethene-based PS which had previously been investigated by MTT assay for the same concentration. The results from the two assays were then compared, and no significant differences were found between the two.

6.3 Future work

The time allotted for this thesis project was limited, and was further impacted by the COVID-19 situation. Consequently, some experimental work remains to be done. Some suggestions for future experiments are listed below.

- A full characterisation of photophysical properties, including quantum yields of fluorescence and singlet oxygen, have to be completed for all chlorins.
- Fluorescence images of the proto-forms in dye-labelled cells should be recorded, for comparison with the Zn-forms. However, more investigations should be carried out to ensure better quality images, and new images should be taken of the Zn-forms, as well. For example, the concentrations of the chlorins could be increased further to reduce the need of amplification of the signal. In this case, one should assess if the resulting images would be representative for a PDT situation.
- Colocalization analysis could be done using Costes' threshold determination, or other accepted unbiased methods, rather than estimating suitable thresholds manually.
- Cell viability assays for dark toxicity, with at least three biological replicates, should be completed for all chlorins.
- The results from the experiments done on the AY27 cell line should be compared with results of similar experiments on a cell line of healthy bladder cells, to investigate if the chlorins show any preference for cancer cells.

Chapter 7

Conclusions

1. Adding sugar groups of glucose, galactose or N-acetyl gluocsamine to the KA20-10.2 chlorin decreased the fluorescence quantum yield, and improved cellular uptake and intracellular distribution in the AY27 bladder cancer cell line.
2. PDT effects in AY27 cells exposed to blue light were limited for KA20-10.2, but greatly increased for all its glycoconjugates.
3. The proto-forms of the chlorins were significantly more effective as PSs in blue-light PDT than their Zn-form counterparts.
4. Only minimal differences in PDT efficiency were found for KA20-11H-proto, 15H-proto and 16H-proto.

Bibliography

[1] James C. Kennedy and Roy H. Pottier. New trends in photobiology: Endogenous protoporphyrin ix, a clinically useful photosensitizer for photodynamic therapy. *Journal of Photochemistry and Photobiology B: Biology*, 14(4):275 – 292, 1992.

[2] Wikipedia. Reactive oxygen species. https://en.wikipedia.org/wiki/Reactive_oxygen_species, 2020. Accessed: 02/07/2020.

[3] M. D. Daniell and J. S. Hill. A history of photodynamic therapy. *Australian and New Zealand Journal of Surgery*, 61(5):340–348, 1991.

[4] Heidi Abrahamse and Michael Hamblin. New photosensitizers for photodynamic therapy. *Biochemical Journal*, 473:347–364, 02 2016.

[5] Dennis E.J.G.J. Dolmans, Dai Fukumura, and Rakesh K. Jain. Photodynamic therapy for cancer. *Nature Reviews Cancer*, 3:380–387, 01 2003.

[6] Vanya Bogoeva, Monica Siksjø, Kristin G. Sæterbø, Thor Bernt Melø, Astrid Bjørkøy, Mikael Lindgren, and Odrun A. Gederaas. Ruthenium porphyrin-induced photodamage in bladder cancer cells. *Photodiagnosis and Photodynamic Therapy*, 14:9 – 17, 2016.

[7] Cristina Cepraga, Thibault Gallavardin, Sophie Marotte, Pierre-Henri Lanoë, J.-C Mulatier, Frederic Lerouge, Stephane Parola, Mikael Lindgren, Patrice Baldeck, Jacqueline Marvel, Olivier Maury, Cyrille Monnereau, Arnaud Favier, Chantal Andraud, Yann Leverrier, and Marie-Therese Charreyre. Biocompatible well-defined chromophore-polymer conjugates for photodynamic therapy and two-photon imaging. *Polymer Chemistry*, 4:61, 01 2013.

[8] Pierre-Henri Lanoë, Thibault Gallavardin, Aurore Dupin, Olivier Maury, Patrice Baldeck, Mikael Lindgren, Cyrille Monnereau, and Chantal Andraud. Influence of bromine substitution pattern on the singlet oxygen generation efficiency of two-photon absorbing chromophores. *Organic & biomolecular chemistry*, 10:6275–8, 06 2012.

[9] Asta Juzeniene. Chlorin e6-based photosensitizers for photodynamic therapy and photodiagnosis. *Photodiagnosis and Photodynamic Therapy*, 6(2):94 – 96, 2009.

[10] Encyclopædia Britannica. Energy state - atomic physics. https://www.britannica.com/science/energy-state. Accessed: 15/12/2019.

[11] Chemistry LibreTexts™. Jablonski diagram. https://chem.libretexts.org/Bookshelves/Physical_and_Theoretical_Chemistry_Textbook_Maps/Supplemental_Modules_(Physical_and_Theoretical_Chemistry)/Spectroscopy/Electronic_Spectroscopy/Jablonski_diagram. Accessed: 17/12/2019.

[12] Joseph Lakowicz. *Principles of Fluorescence Spectroscopy*. Kluwer Academic/Plenum Publishers, 2nd edition, 1999.

[13] Ana Castano, Tatiana Demidova, and Michael Hamblin. Mechanisms in photodynamic therapy: Part three - photosensitizer pharmacokinetics, biodistribution, tumor localization and modes of tumor destruction. *Photodiagnosis Photodyn Ther*, 2:91–106, 06 2005.

[14] Michael R. Hamblin and E. Luke Newman. New trends in photobiology: On the mechanism of the tumour-localising effect in photodynamic therapy. *Journal of Photochemistry and Photobiology B: Biology*, 23(1):3 – 8, 1994.

[15] Alicja Jozkowicz, Halina Was, and Jozef Dulak. Heme oxygenase-1 in tumors: Is it a false friend? *Antioxidants & redox signaling*, 9:2099–117, 01 2008.

[16] Zvi Malik and Meir Djaldetti. Destruction of erythroleukemia, myelocytic leukemia and burkitt lymphoma cells by photoactivated protoporphyrin. *International journal of cancer*, 26 4:495–500, 1980.

[17] Eun Ji Hong, Dae Gun Choi, and Min Shim. Targeted and effective photodynamic therapy for cancer using functionalized nanomaterials. *Acta Pharmaceutica Sinica B*, 6, 04 2016.

[18] Pawel Swietach, Richard Vaughan-Jones, Adrian Harris, and Alzbeta Hulikova. The chemistry, physiology and pathology of ph in cancer. *Philosophical transactions of the Royal Society of London. Series B, Biological sciences*, 369:20130099, 02 2014.

[19] Sandy Azzi, Jagoda Hebda, and Julie Gavard. Vascular permeability and drug delivery in cancers. *Frontiers in oncology*, 3:211, 08 2013.

[20] Michael Hockel and Peter Vaupel. Tumor Hypoxia: Definitions and Current Clinical, Biologic, and Molecular Aspects. *JNCI: Journal of the National Cancer Institute*, 93(4):266–276, 02 2001.

[21] Maria V. Liberti and Jason W. Locasale. The warburg effect: How does it benefit cancer cells? *Trends in Biochemical Sciences*, 41(3):211 – 218, 2016. Special Issue: Mitochondria & Metabolism.

[22] Odrun Gederaas, Anders Johnsson, Kristian Berg, Manandhar Rojlina, Chetana Shrestha, Daniel Skåre, Ingvild Ekroll, Anders Høgset, and Astrid Hjelde. Photochemical internalization in bladder cancer – development of an orthotopic in vivo model. *Photochem. Photobiol. Sci.*, 16, 09 2017.

[23] K Plaetzer, B Krammer, Jürgen Berlanda, Frieder Berr, and Tobias Kiesslich. Photophysics and photochemistry of photodynamic therapy: Fundamental aspects. *Lasers in medical science*, 24:259–68, 03 2008.

[24] Patrizia Agostinis, Kristian Berg, Keith A Cengel, Thomas H. Foster, Albert W. Girotti, Sandra O Gollnick, Stephen M. Hahn, Michael R. Hamblin, Asta Juzeniene, David Kessel, Mladen Korbelik, Johan Emelian Moan, Pawel Mróz, Dominika Nowis, Jacques Piette, Brian Wilson, and Jakub Gołąb. Photodynamic therapy of cancer: an update. *CA: a cancer journal for clinicians*, 61 4:250–81, 2011.

[25] Eivind Larsen, Lise Lyngsnes Randeberg, Odrun Gederaas, Carl-Jørgen Arum, Astrid Hjelde, Chun-Mei Zhao, Chen Duan, Hans Krokan, and Lars Svaasand. Monitoring of hexyl 5-aminolevulinate-induced photodynamic therapy in rat bladder cancer by optical spectroscopy. *Journal of biomedical optics*, 13:044031, 07 2008.

[26] Dominika Nowis, Marcin Makowski, Tomasz Stokłosa, Magdalena Legat, Tadeusz Issat, and Jakub Golab. Direct tumor damage mechanisms of photodynamic therapy. *Acta biochimica Polonica*, 52:339–52, 02 2005.

[27] Wikipedia. Reactive nitrogen species. https://en.wikipedia.org/wiki/Reactive_nitrogen_species, 2020. Accessed: 02/07/2020.

[28] Hee Sook Hwang, Heejun Shin, Jieun Han, and Kun Na. Combination of photodynamic therapy (pdt) and anti-tumor immunity in cancer therapy. *Journal of Pharmaceutical Investigation*, 48(2):143–151, Mar 2018.

[29] Johan Moan and Kristian Berg. The photodegradation of porphyrins in cells can be used to estimate the lifetime of singlet oxygen. *Photochemistry and Photobiology*, 53(4):549–553, 1991.

[30] Defeng Wu and Arthur Cederbaum. Alcohol, oxidative stress, and free radical damage. *Alcohol research & health : the journal of the National Institute on Alcohol Abuse and Alcoholism*, 27:277–84, 01 2003.

[31] Anne C.E Moor. Signaling pathways in cell death and survival after photodynamic therapy. *Journal of Photochemistry and Photobiology B: Biology*, 57(1):1 – 13, 2000.

[32] Maureen Redza-Dutordoir and Diana A. Averill-Bates. Activation of apoptosis signalling pathways by reactive oxygen species. *Biochimica et Biophysica Acta (BBA) - Molecular Cell Research*, 1863(12):2977 – 2992, 2016.

[33] Charles J. Gomer, Natalie Rucker, and A. Linn Murphree. Differential cell photosensitivity following porphyrin photodynamic therapy. *Cancer Research*, 48(16):4539–4542, 1988.

[34] Ana P. Castano, Pawel Mroz, and Michael R. Hamblin. Photodynamic therapy and anti-tumour immunity. *Nature Reviews Cancer*, 6(7):535–545, 7 2006.

[35] Laura Milla Sanabria, Matías Exequiel Rodríguez, Ingrid Sol Cogno, Natalia Belén Rumie Vittar, María Florencia Pansa, María Julia Lamberti, and Viviana Alicia Rivarola. Direct and indirect photodynamic therapy effects on the cellular and molecular components of the tumor microenvironment. *Biochimica et Biophysica Acta (BBA) - Reviews on Cancer*, 1835(1):36 – 45, 2013.

[36] Steen Steenken and Slobodan V. Jovanovic. How easily oxidizable is dna? one-electron reduction potentials of adenosine and guanosine radicals in aqueous solution. *Journal of the American Chemical Society*, 119(3):617–618, 1997.

[37] Lucymara F. Agnez-Lima, Julliane T.A. Melo, Acarízia E. Silva, Ana Helena S. Oliveira, Ana Rafaela S. Timoteo, Keronninn M. Lima-Bessa, Glaucia R. Martinez, Marisa H.G. Medeiros, Paolo [Di Mascio], Rodrigo S. Galhardo, and Carlos F.M. Menck. Dna damage by singlet oxygen and cellular protective mechanisms. *Mutation Research/Reviews in Mutation Research*, 751(1):15 – 28, 2012.

[38] Carlos Frederico Martins Menck, Paolo di Mascio, L F Agnez, Denise T. Ribeiro, and Regina Costa de Oliveira. Genetic deleterious effects of singlet oxygen. 1993.

[39] Cooper GM. *The Cell: A Molecular Approach*. Sunderland (MA): Sinauer Associates, 2nd edition, 2000.

[40] Wikimedia Commons. Cell cycle. https://commons.wikimedia.org/wiki/File:Cell_Cycle_2-2.svg, 2006. Accessed: 18/12/2019.

[41] Jennifer A. Seiler, Chiara Conti, Ali Syed, Mirit I. Aladjem, and Yves Pommier. The intra-s-phase checkpoint affects both dna replication initiation and elongation: Single-cell and -dna fiber analyses. *Molecular and Cellular Biology*, 27(16):5806–5818, 2007.

[42] Carol Bernstein, Anil R. Prasad, Valentine Nfonsam, and Harris Bernstein. Dna damage, dna repair and cancer, new research directions in dna repair. *IntechOpen*, 2013.

[43] John F. R. Kerr, Clay M. Winterford, and Brian V. Harmon. Apoptosis. its significance in cancer and cancer therapy. *Cancer*, 73(8):2013–2026, 1994.

[44] Sergey Y.a Proskuryakov, Anatoli G Konoplyannikov, and Vladimir L Gabai. Necrosis: a specific form of programmed cell death? *Experimental Cell Research*, 283(1):1 – 16, 2003.

[45] Chemistry LibreTexts™. The Beer-Lambert law. https://chem.libretexts.org/Bookshelves/Physical_and_Theoretical_Chemistry_Textbook_Maps/Supplemental_Modules_(Physical_and_Theoretical_Chemistry)/Spectroscopy/Electronic_Spectroscopy/Electronic_Spectroscopy_Basics/The_Beer-Lambert_Law. Accessed: 17/12/2019.

[46] Knut Rurack and Monika Spieles. Fluorescence quantum yields of a series of red and near-infrared dyes emitting at 600-1000 nm. *Analytical chemistry*, 83(4):1232—1242, February 2011.

[47] Mikhail Berezin and Samuel Achilefu. Fluorescence lifetime measurements and biological imaging. *Chemical reviews*, 110:2641–84, 03 2010.

[48] Biology LibreTexts™. Instruments of microscopy. https://bio.libretexts.org/Bookshelves/Microbiology/Book%3A_Microbiology_(OpenStax)/02+%3A_How_We_See_the_Invisible_World/2.3%3A_Instruments_of_Microscopy. Accessed: 18/12/2019.

[49] Thomas J. Fellers and Michael W. Davidson. Introduction to confocal microscopy. https://www.olympus-lifescience.com/en/microscope-resource/primer/techniques/confocal/confocalintro/. Accessed: 29/03/2020.

[50] Kenneth W. Dunn, Malgorzata M. Kamocka, and John H. McDonald. A practical guide to evaluating colocalization in biological microscopy. *American Journal of Physiology-Cell Physiology*, 300(4):C723–C742, 2011. PMID: 21209361.

[51] Wikimedia Commons. Dividing cell fluorescence. https://commons.wikimedia.org/wiki/File:Dividing_Cell_Fluorescence.jpg, 2010. Accessed: 03/04/2020.

[52] Jonathan W.D. Comeau, Santiago Costantino, and Paul W. Wiseman. A guide to accurate fluorescence microscopy colocalization measurements. *Biophysical Journal*, 91(12):4611 – 4622, 2006.

[53] Jesse S. Aaron, Aaron B. Taylor, and Teng-Leong Chew. Image co-localization – co-occurrence versus correlation. *Journal of Cell Science*, 131(3), 2018.

[54] E. M. Manders, F. J. Verbeek, and J. A. Aten. Measurement of co-localization of objects in dual-colour confocal images. *Journal of Microscopy*, 169(3):375–382, 1993.

[55] E.M. Manders, J. Stap, G.J. Brakenhoff, R. van Driel, and J.A. Aten. Dynamics of three-dimensional replication patterns during the s-phase, analysed by double labelling of dna and confocal microscopy. *Journal of Cell Science*, 103(3):857–862, 1992.

[56] C. Spearman. "general intelligence," objectively determined and measured. *The American Journal of Psychology*, 15(2):201–292, 1904.

[57] Qi Li, Anthony Lau, Terence J. Morris, Lin Guo, Christopher B. Fordyce, and Elise F. Stanley. A syntaxin 1, g, and n-type calcium channel complex at a presynaptic nerve terminal: Analysis by quantitative immunocolocalization. *Journal of Neuroscience*, 24(16):4070–4081, 2004.

[58] Fabrice P. Cordelières and Susanne Bolte. Jacop documentation. https://imagej.nih.gov/ij/plugins/track/jacop2.html, 2006. Accessed: 17/04/2020.

[59] Sylvain Costes, Dirk Daelemans, Edward Cho, Zachary Dobbin, George Pavlakis, and Stephen Lockett. Automatic and quantitative measurement of protein-protein colocalization in live cells. *Biophysical journal*, 86:3993–4003, 07 2004.

[60] Bradley Efron and Robert J. Tibshirani. *An Introduction to the Bootstrap*. Chapman & Hall, 1993.

[61] Bradley Efron. Nonparametric standard errors and confidence intervals. *Canadian Journal of Statistics*, 9(2):139–158, 1981.

[62] Ben David Normann. Gauss' law of error propagation explained. https://penofben.files.wordpress.com/2016/02/gausserrorpropagation2.pdf, 2016. Accessed: 28/06/2020.

[63] A. M. Brouwer. Standards for photoluminescence quantum yield measurements in solution. *Pure and Applied Chemistry*, 83(12):2213–2228, 2011.

[64] John O'Brien, Ian Wilson, Terry Orton, and François Pognan. Investigation of the alamar blue (resazurin) fluorescent dye for the assessment of mammalian cell cytotoxicity. *European Journal of Biochemistry*, 267(17):5421–5426, 2000.

[65] Wei Zhu, Ying-Hua Gao, Ping-Yong Liao, Dan-Ye Chen, Ning-Ning Sun, Anh Nguyen Thi, Yi-Jia Yan, Xiao-Feng Wu, and Zhi-Long Chen. Comparison between porphin, chlorin and bacteriochlorin derivatives for photodynamic therapy: Synthesis, photophysical properties, and biological activity. *European Journal of Medicinal Chemistry*, 160, 10 2018.

[66] Nelson A.M. Pereira, Mafalda Laranjo, João Pina, Andreia S.R. Oliveira, João Dias Ferreira, Carles Sánchez-Sánchez, João Casalta-Lopes, Ana Cristina Gonçalves, Ana Bela Sarmento-Ribeiro, Marta Piñeiro, J. Sérgio [Seixas de Melo], Maria Filomena Botelho, and Teresa M.V.D. [Pinho e Melo]. Advances on photodynamic therapy of melanoma through novel ring-fused 5,15-diphenylchlorins. *European Journal of Medicinal Chemistry*, 146:395 – 408, 2018.

[67] Katriann Arja, Mathias Elgland, Hanna Appelqvist, Peter Konradsson, Mikael Lindgren, and Peter Nilsson. Synthesis and characterization of novel fluoroglycosylated porphyrins that can be utilized as theranostic agents. *ChemistryOpen*,

7(7):495–503, 2018. Funding Agencies|Swedish Foundation for Strategic Research; Swedish Research Council.

[68] Mikkel Bregnhøj, Michael Westberg, Frank Jensen, and Peter R. Ogilby. Solvent-dependent singlet oxygen lifetimes: temperature effects implicate tunneling and charge-transfer interactions. *Phys. Chem. Chem. Phys.*, 18:22946–22961, 2016.

[69] Anish Prasanna, Mansoor M Ahmed, Mohammed Mohiuddin, and C Norman Coleman. Exploiting sensitization windows of opportunity in hyper and hypo-fractionated radiation therapy. *Journal of thoracic disease*, 6(4):287—302, April 2014.

[70] Brian Marples and Spencer J. Collis. Low-dose hyper-radiosensitivity: Past, present, and future. *International Journal of Radiation Oncology*Biology*Physics*, 70(5):1310 – 1318, 2008.

[71] Oluwole Olobatuyi, Gerda de Vries, and Thomas Hillen. A reaction-diffusion model for radiation-induced bystander effects. *bioRxiv*, 2016.

[72] Upadhyayula Sai Srinivas, Bryce W.Q. Tan, Balamurugan A. Vellayappan, and Anand D. Jeyasekharan. Ros and the dna damage response in cancer. *Redox Biology*, 25:101084, 2019. Redox Regulation of Cell State and Fate.

[73] PhotochemCAD. Chlorin e6. http://www.photochemcad.com/compound-detail.php?name=Chlorin%20e6, 2004. Accessed: 23/06/2020.

[74] Ahmad Amirshaghaghi, Lesan Yan, Joann Miller, Yonathan Daniel, Joel Stein, Theresa Busch, Zhiliang Cheng, and Andrew Tsourkas. Chlorin e6-coated superparamagnetic iron oxide nanoparticle (spion) nanoclusters as a theranostic agent for dual-mode imaging and photodynamic therapy. *Scientific Reports*, 9, 12 2019.

[75] James Carmichael, William G. DeGraff, Adi F. Gazdar, John D. Minna, and James B. Mitchell. Evaluation of a tetrazolium-based semiautomated colorimetric assay: Assessment of chemosensitivity testing. *Cancer Research*, 47(4):936–942, 1987.

Appendices

Appendix A

Synthetic schemes

Figures A.1, A.2 and A.3 show the synthetic schemes for the preparation of the chlorin compounds studied in the thesis. Figure A.4 show enlarged chemical structures of the final chlorin compounds. All schemes and structures were provided by Dr. Katriann Arja, Linköping University.

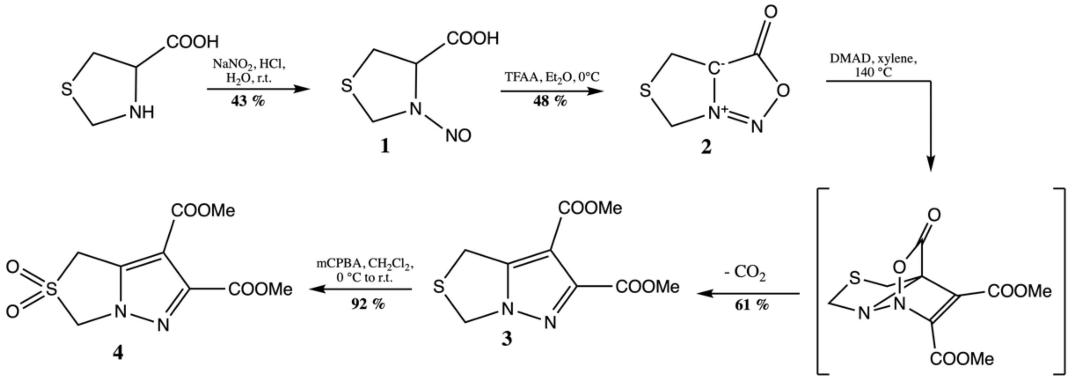
COOH
S
NH
$NaNO_2$, HCl,
H_2O, r.t.
43 %
COOH
S
N
NO
1
TFAA, Et_2O, 0°C
48 %
O
S
C⁻
N+
O
N
2
DMAD, xylene,
140 °C
O
O
S
N
N
COOMe
COOMe
- CO_2
61 %
COOMe
S
N
N
COOMe
3
mCPBA, CH_2Cl_2,
0 °C to r.t.
92 %
COOMe
O
S
O
N
N
COOMe
4

Figure A.1: Scheme 1. Synthesis of S,S-dioxo-pyrazolothiazole 4.

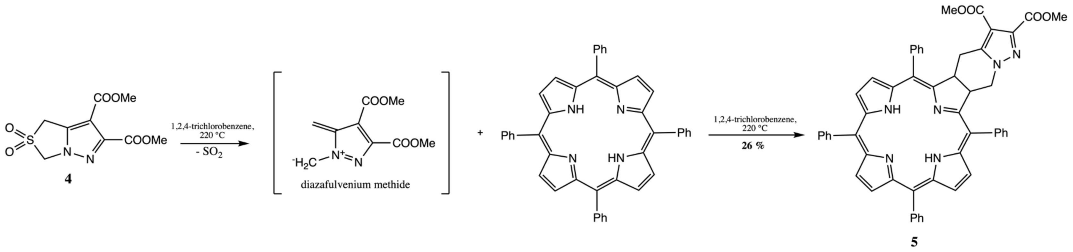
4
1,2,4-trichlorobenzene, 220 °C
- SO2
diazafulvenium methide
1,2,4-trichlorobenzene, 220 °C
26 %
5

Figure A.2: Scheme 2. Synthesis of 4,5,6,7-tetrahydropyrazolo[1,5-a]pyridine fused chlorin 5 (KA20-10.2).

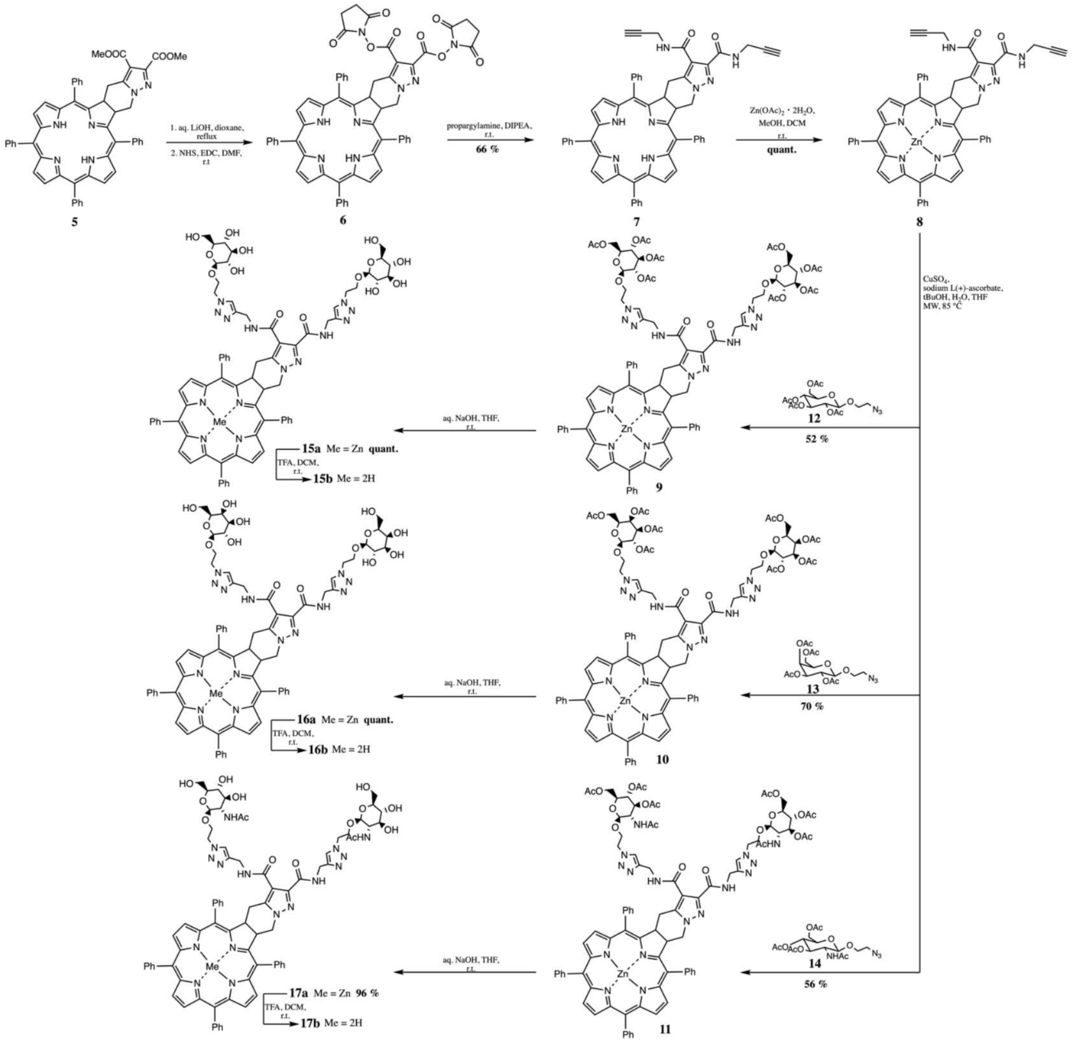
5
1. aq. LiOH, dioxane, reflux
2. NHS, EDC, DMF, r.t.
6
propargylamine, DIPEA, r.t.
66 %
7
Zn(OAc)2 · 2H2O, MeOH, DCM r.t.
quant.
8
CuSO4, sodium L(+)-ascorbate, tBuOH, H2O, THF MW, 85 °C
12
52 %
9
aq. NaOH, THF, r.t.
15a Me = Zn quant.
TFA, DCM, r.t.
15b Me = 2H
13
70 %
10
aq. NaOH, THF, r.t.
16a Me = Zn quant.
TFA, DCM, r.t.
16b Me = 2H
14
56 %
11
aq. NaOH, THF, r.t.
17a Me = Zn 96 %
TFA, DCM, r.t.
17b Me = 2H

Figure A.3: Scheme 3. Synthesis of glycoconjugates of KA20-10.2.

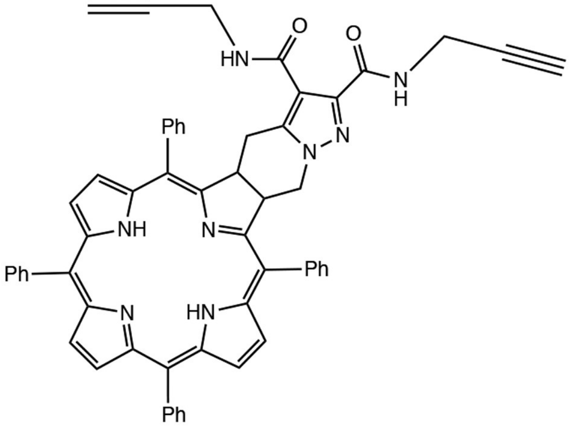
O
O
HN
N
H
Ph
N
N
NH
N
Ph
Ph
N
HN
Ph

KA20-10.2

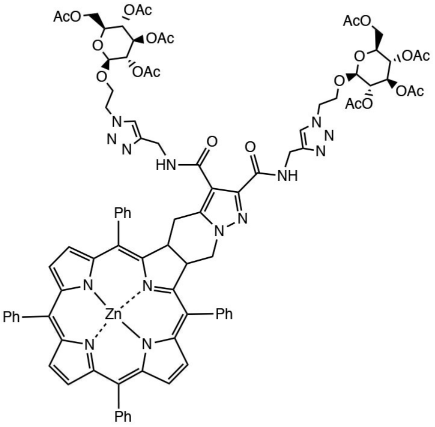
AcO
OAc
OAc
O
OAc
O
AcO
O
OAc
OAc
O
AcO
N
N
N
N
N
N
O
O
HN
NH
Ph
N
N
N
Zn
Ph
Ph
N
N
Ph

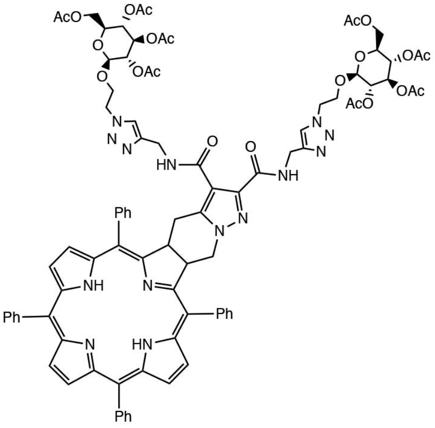
AcO
OAc
OAc
O
OAc
O
AcO
O
OAc
OAc
O
AcO
N
N
N
N
N
N
O
O
HN
NH
Ph
N
N
NH
N
Ph
Ph
N
HN
Ph

KA20-11H **KA20-11H-proto**

Figure A.4

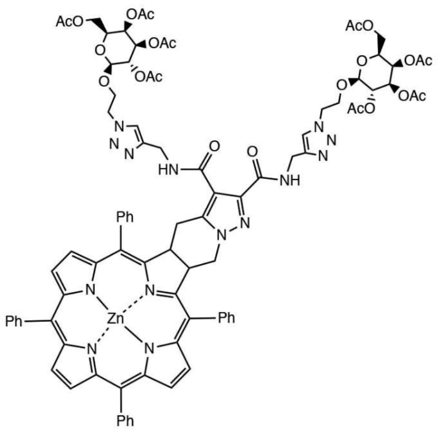
AcO
OAc
OAc
O
OAc
O
N
N
N
HN
O
O
NH
N
N
N
AcO
O
OAc
OAc
AcO
O
Ph
N
N
N
N
Zn
N
N
Ph
Ph
Ph

KA20-15H

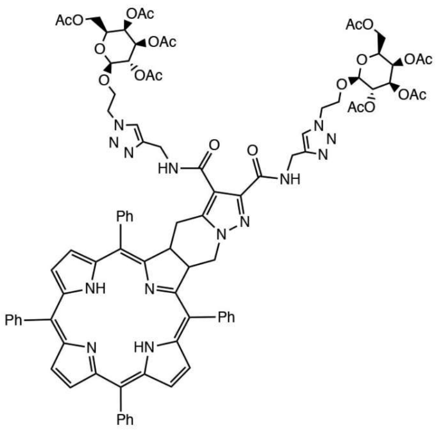
AcO
OAc
OAc
O
OAc
O
N
N
N
HN
O
O
NH
N
N
N
AcO
O
OAc
OAc
AcO
O
Ph
N
N
NH
N
N
HN
Ph
Ph
Ph

KA20-15H-proto

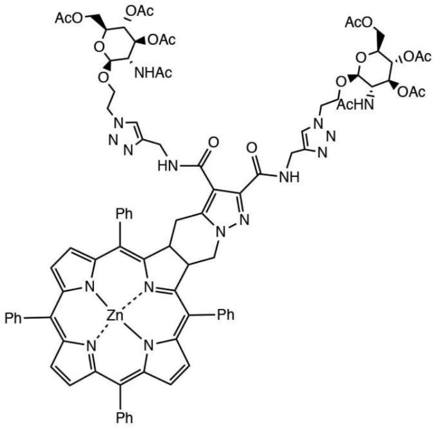
AcO
OAc
OAc
O
NHAc
O
N
N
N
HN
O
O
NH
N
N
N
AcO
O
OAc
OAc
AcHN
O
Ph
N
N
N
N
Zn
N
N
Ph
Ph
Ph

KA20-16H

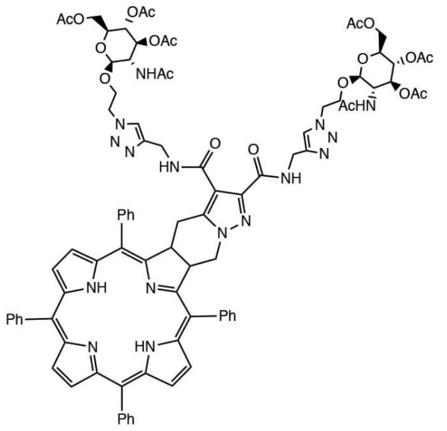
AcO
OAc
OAc
O
NHAc
O
N
N
N
HN
O
O
NH
N
N
N
AcO
O
OAc
OAc
AcHN
O
Ph
N
N
NH
N
N
HN
Ph
Ph
Ph

KA20-16H-proto

Figure A.4: Chemical structures of the chlorins studied in the thesis. Provided by Dr. Katriann Arja, Linköping University.

Appendix B

Bürker chamber

Prior to seeding in dishes or wells, a Bürker chamber was used to manually count the cancer cells (Figure B.1).

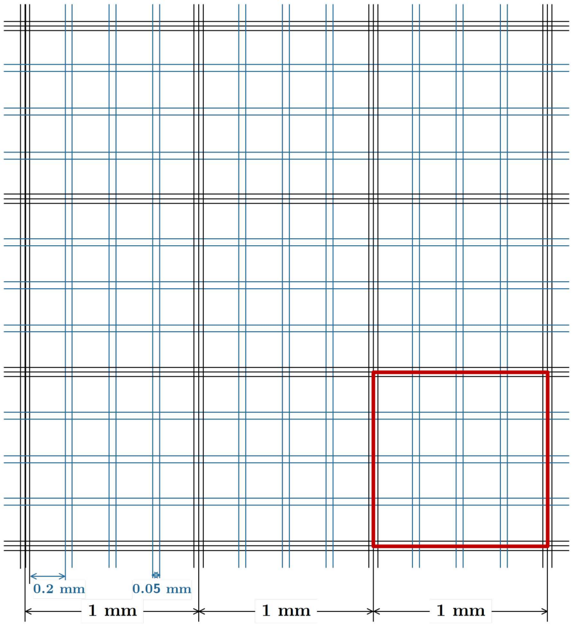

Figure B.1: Sketch of a Bürker chamber used for cell counting. One chamber consists of 3x3 A-squares, marked in red. Each A-square is 1 mm × 1 mm × 0.1 mm, giving a volume of 0.1 μL per square. (Figure drawn by B. Vindstad, 2020)

To determine the number of cells per mL, at least three A-squares (marked in red in figure B.1) were counted. Each square contains 0.1 μL of cell suspension, giving the following formula for cell concentration:

$$N_c = \frac{N}{N_A \cdot 0.1 \cdot 10^6} = \frac{N \cdot 10^4}{N_A} \tag{B.1}$$

where N_c is the number of cells per mL in the cell suspension, N is the total number of cells counted and N_A is the number of A-squares counted.

Appendix C

Images and script used in colocalization analysis

Images C.1 through C.4 show all images used in the colocalization analysis of chlorins KA20-10.2, KA20-11H and KA20-16H. Images were stained with CellMaks Green, LysoTracker Blue or Draq5 dyes, marking the cell membrane, lysosomes or nuclei of the cells. All images were taken in a Leica TCS SP8 MP confocal laser scanning microscope. Figure C.5 shows the script used to calculate the coefficients used in the thesis (overlap percentage, MCC), written in the Python 3 programming language.

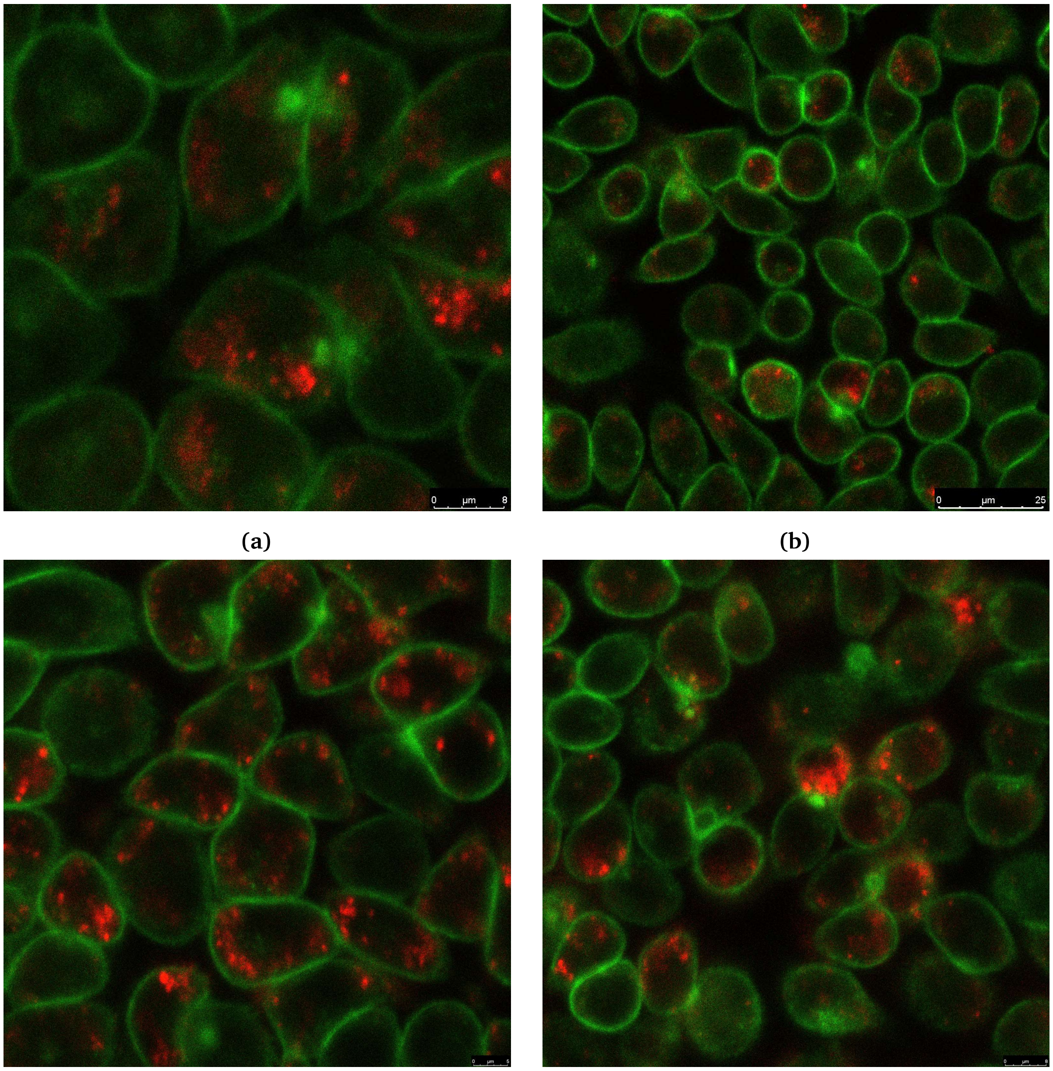

(a) **(b)**

(c) **(d)**

Figure C.1: Fluorescence images of AY27 cells incubated with KA20-10.2 (1 µM, 24 h, 37 °C) and stained with CellMask Green, taken in a CLSM microscope.

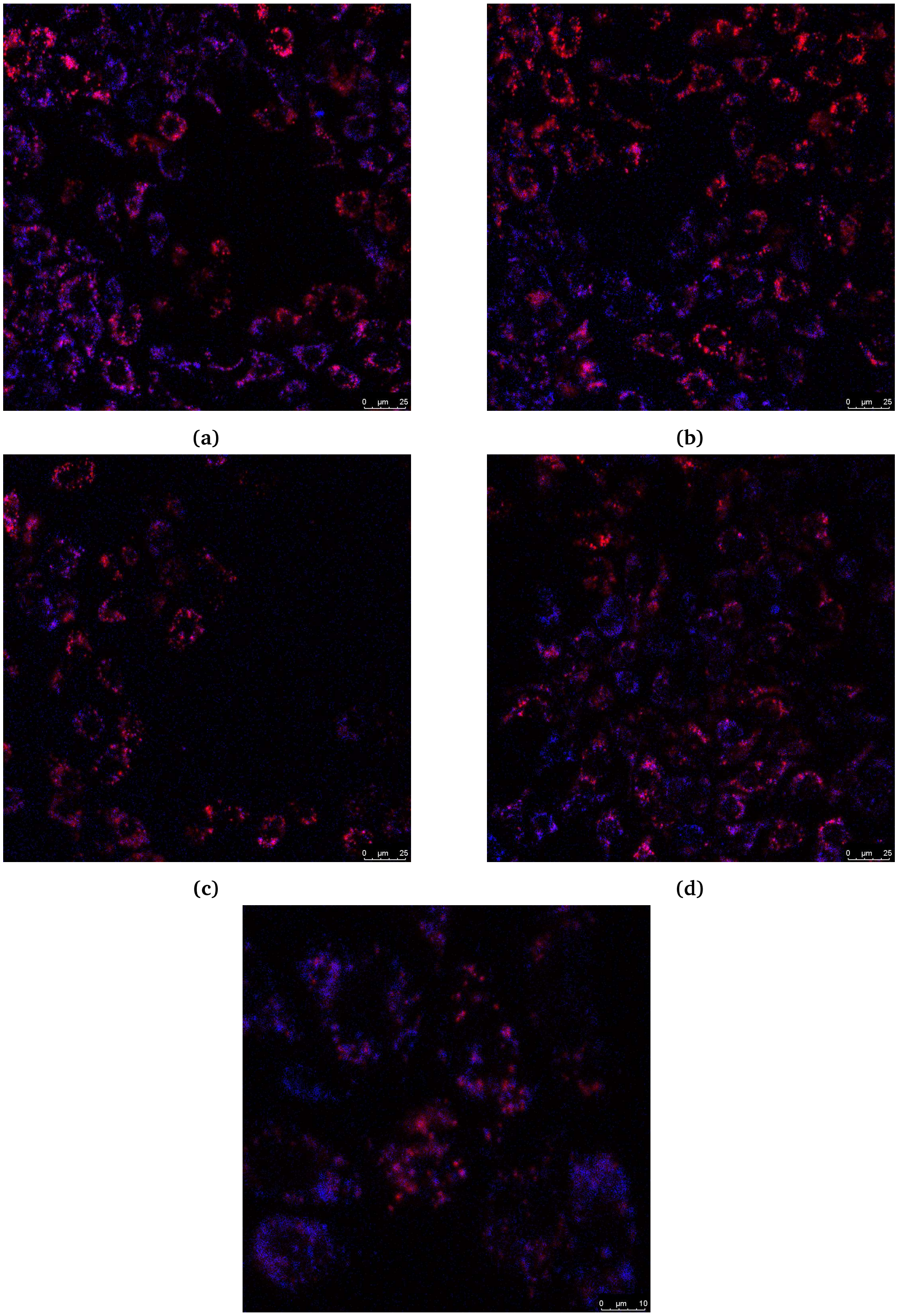
0 µm 25
0 µm 25
0 µm 25
0 µm 25
0 µm 10

(a) (b) (c) (d) (e)

Figure C.2: Fluorescence images of AY27 cells incubated with KA20-10.2 (1 µM, 24 h, 37 °C) and stained with LysoTracker Blue, taken in a CLSM microscope.

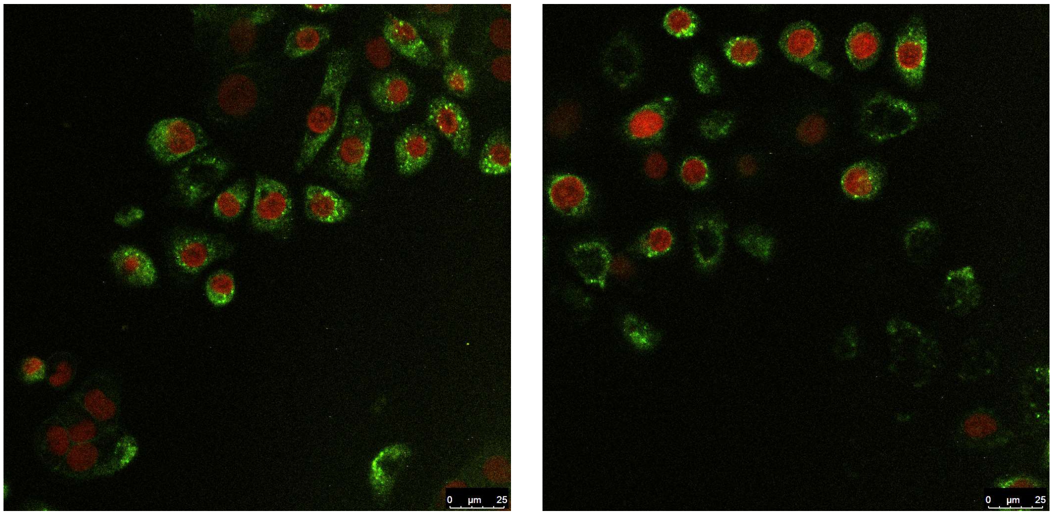

(a) **(b)**

Figure C.3: Fluorescence images of AY27 cells incubated with KA20-11H (10 µM, 24 h, 37 °C) and stained with Draq5, taken in a CLSM microscope.

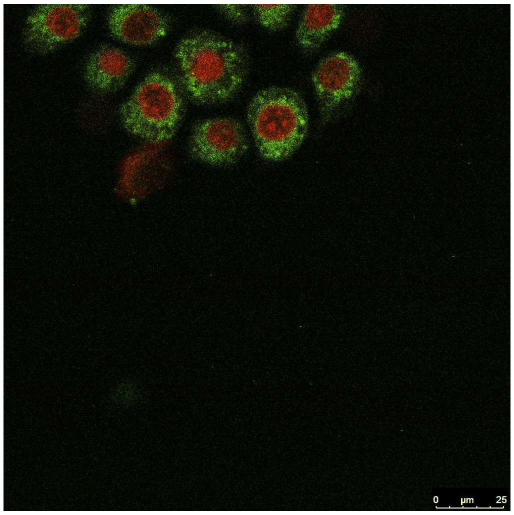

(a)

Figure C.4: Fluorescence image of AY27 cells incubated with KA20-16H (10 µM, 24 h, 37 °C) and stained with Draq5, taken in a CLSM microscope.

```python
# D:\Master\scripts\Colocalization\Overlap-MCC-Cooccurrence.py
import cv2
import numpy as np
from tkinter import Tk
from tkinter.filedialog import askopenfilename

def nothing(x):
  pass

root = Tk()
root.withdraw()
root.wm_attributes('-topmost', 1)

## read image, separate channels
filename1 = askopenfilename() # show an "Open" dialog box and return the path to the selected file
image = cv2.imread(filename1)
image = cv2.resize(image, (512,512), interpolation = cv2.INTER_AREA)

red_channel = image[:,:,2]
channel2='green' #choose color of second channel
if channel2=='blue':
    second_channel = image[:,:,0]
elif channel2=='green':
    second_channel = image[:,:,1]

## find average of all nonzero values
red_channel_copy=image[:,:,2]
second_channel_copy=second_channel

red_mask = np.ma.masked_equal(red_channel_copy,0)
second_mask = np.ma.masked_equal(second_channel_copy,0)
redmean = np.mean(red_mask)
secondmean= np.mean(second_mask)

## manually set threshold for both channels
cv2.namedWindow('Colorbars')
hh='Threshold'
wnd='Colorbars'

cv2.createTrackbar("Threshold", "Colorbars",0,100,nothing) #create trackbar for threshold value
refimg = cv2.resize(red_channel, (0,0), fx=0.5, fy=0.5) #reference (no threshold) image
Image1 = cv2.resize(red_channel, (0,0), fx=0.5, fy=0.5) #thresholded image
cv2.imshow('FirstImgTitle',refimg)

while(1):
    hul1=cv2.getTrackbarPos("Threshold", "Colorbars") #get trackbar position
    ret,thresh_red = cv2.threshold(red_channel,hul1,255,cv2.THRESH_TOZERO) #set threshold to trackbar value, get threshold value
    cv2.imshow("thresh1",thresh_red) #update thresholded image
    k = cv2.waitKey(1) & 0xFF
    if k == 27: #repeat until ESC is pressed
        break
cv2.destroyAllWindows()

#repeat for second channel
cv2.namedWindow('Colorbars')
cv2.createTrackbar("Threshold", "Colorbars",0,100,nothing)
refimg = cv2.resize(second_channel, (0,0), fx=0.5, fy=0.5)
Image2 = cv2.resize(second_channel, (0,0), fx=0.5, fy=0.5)
cv2.imshow('SecondChannel',refimg)

```

Figure C.5: Script used for calculation MCC and simple area analysis overlap percentage, page 1. Written in the Python 3 programming language.

```python
while(1):
    hul2=cv2.getTrackbarPos("Threshold", "Colorbars")
    ret,thresh_second = cv2.threshold(second_channel,hul2,255,cv2.THRESH_TOZERO)
    cv2.imshow("thresh2",thresh_second)
    k = cv2.waitKey(1) & 0xFF
    if k == 27:
        break
cv2.destroyAllWindows()

## find overlap of thresholded images and calculate overlap percentage
img1_nonzero_after_thresh = np.nonzero(thresh_red)
img2_nonzero_after_thresh = np.nonzero(thresh_second)

img1_tuple_1st = img1_nonzero_after_thresh[0]
img2_tuple_1st = img2_nonzero_after_thresh[0]

Image1Value= len(img1_tuple_1st) #total number of non-zero pixels, channel 1
Image2Value= len(img2_tuple_1st) #total number of non-zero pixels, channel 2

multipliedmatrix = np.multiply(thresh_red,thresh_second) #multiply to set all non-overlap pixels to zero
nonzero = np.nonzero(multipliedmatrix)
ColocValue=len(nonzero[0]) #find number of resulting non-zero (=overlap) pixels

OverlapCalc= ((ColocValue/(Image1Value+Image2Value-ColocValue))*100) #calculate overlap percentage

## iterate over thresholded channels and calculate MCC
M1num=0
M2num=0
M1den=0
M2den=0

for i in range(len(red_channel)):
    for j in range(len(red_channel[i])):

        M1den=M1den+thresh_red[i,j]
        M2den=M2den+thresh_second[i,j]

        if thresh_red[i,j] != 0 and thresh_second[i,j] != 0:

            M1num=M1num+red_channel[i,j]
            M2num=M2num+second_channel[i,j]

M1calc=M1num/M1den
M2calc=M2num/M2den

## print resulting values
print("Overlap percentage: " + str(OverlapCalc))
print("M1 value: " + str(M1calc))
print("M2 value: " + str(M2calc))

root.destroy()
```

Figure C.5: Script used for calculation MCC and simple area analysis overlap percentage, page 2. Written in the Python 3 programming language.

Appendix D

Additional results

Figures D.1 through D.3 show the results for PDT experiments from all tested concentrations of KA20-10.2, KA20-11H and KA20-11H-proto. The control (light only) group in these figures are the overall average values of all experiments.

Figure D.4 show the results from a viability assay on AY27 cells incubated with KA20-11H-proto or KA20-16H-proto, with concentrations ranging from 0.05 µM to 100 µM.

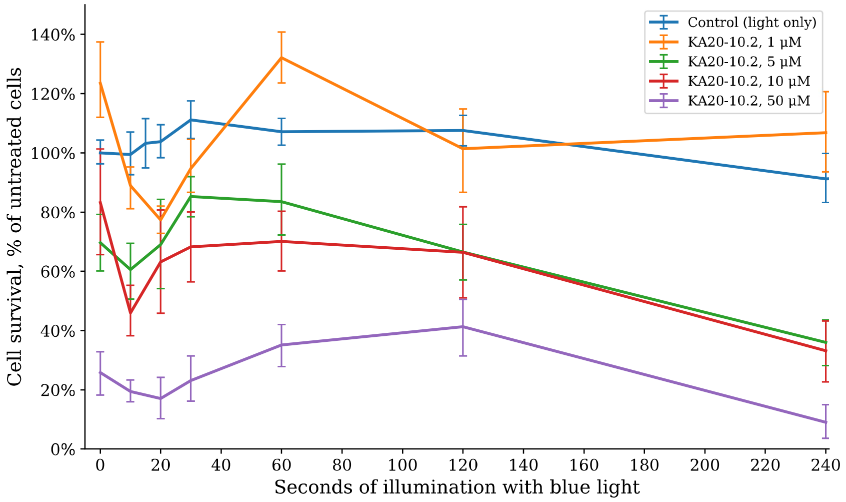

Figure D.1: The relative cell survival of AY27 cells after treatment with various concentrations of KA20-10.2 and blue light (435 nm), or light only, compared to untreated cells. The error bars show the 95 % confidence interval of the mean values.

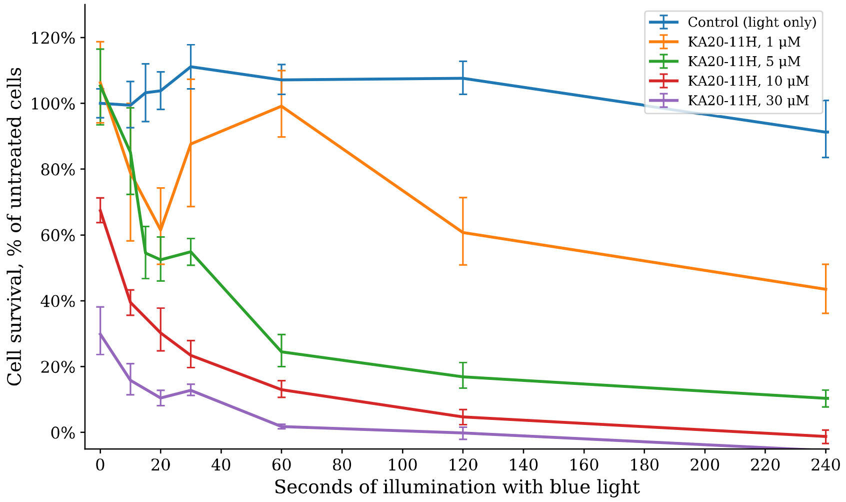

Figure D.2: The relative cell survival of AY27 cells after treatment with various concentrations of KA20-11H and blue light (435 nm), or light only, compared to untreated cells. The error bars show the 95 % confidence interval of the mean values.

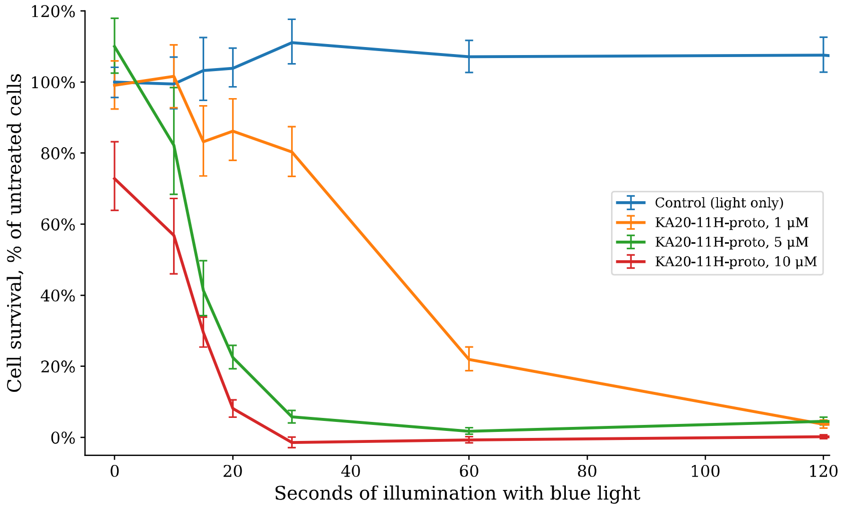

Figure D.3: The relative cell survival of AY27 cells after treatment with various concentrations of KA20-11H-proto and blue light (435 nm), or light only, compared to untreated cells. The error bars show the 95 % confidence interval of the mean values.

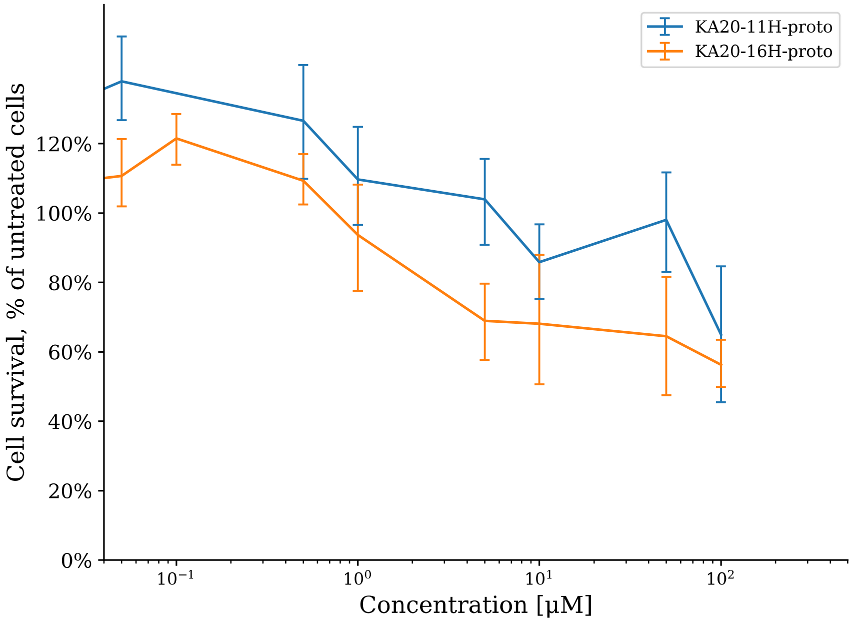

Figure D.4: The relative cell survival of AY27 cells incubated with various concentrations of KA20-11H-proto and KA20-16H-proto, compared to untreated cells.

Appendix E

Complementary measurements

Complementary photo-physical measurements performed by Prof. M. Lindgren, Department of Physics, NTNU are presented in Figures E.1 through E.4.

Figure E.1 shows measurements of transient singlet oxygen luminescence cefore and after Argon-bubbling treatment. Initially, a singlet oxygen signal is present (black curve). Upon flushing the sample cell with Argon for 8 min, and thus removing oxygen from the sample, the signal diminishes (red curve). After subsequently opening the sample cell for air, allowing oxygen to re-enter the sample, the singlet oxygen signal reappears (blue curve).

Figure E.2 shows measurements of transient singlet oxygen luminescence for KA20-11H-proto in different solvents. The resulting lifetimes, varying from 10.9 µs to 206 µs, are presented in Table E.1. Figure E.3 shows the absorbance spectra of KA20-11H-proto for the different solvents used in Figure E.2.

Figure E.4 show measurements of singlet oxygen signal of KA20-15H and KA20-15H-proto. These measurements, together with measurements of reference molecule phenatrone, were used to determine the singlet oxygen QYs to 68 % for both the Zn-form and proto-form of the chlorin.

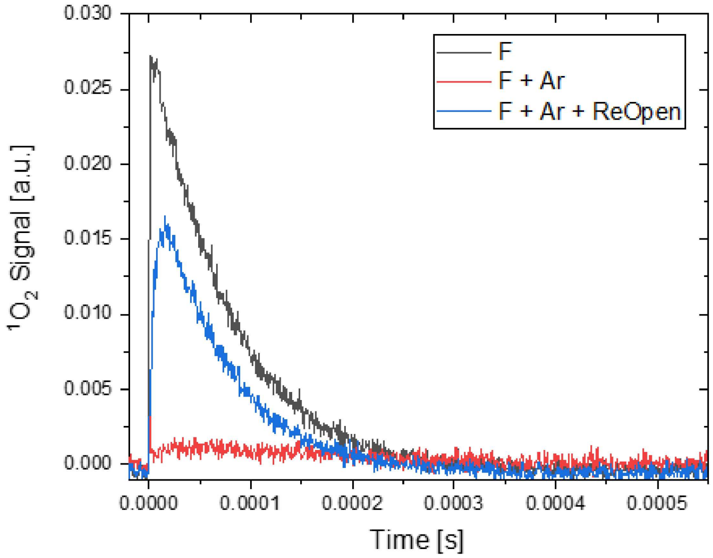

Figure E.1: Transient singlet oxygen luminescence of KA20-11H (denoted "F") for different Ar-bubbling treatments, using Acetonitrile (ACN) as solvent. The chlorin is excited at 594 nm in the Q-band, and the concentration is approx. 6 µM.

Table E.1: Results for the lifetimes τ of singlet oxygen luminescence of KA20-11H-proto in different solvents, found from the exponential fit of the curves in Figure E.2.

Solvent	Excitation wavelength [nm]	Lifetime τ [µs]
ACN	594	87.6 ± 0.5
CHCI3	596	206 ± 1
MeOH	540	10.9 ± 0.07

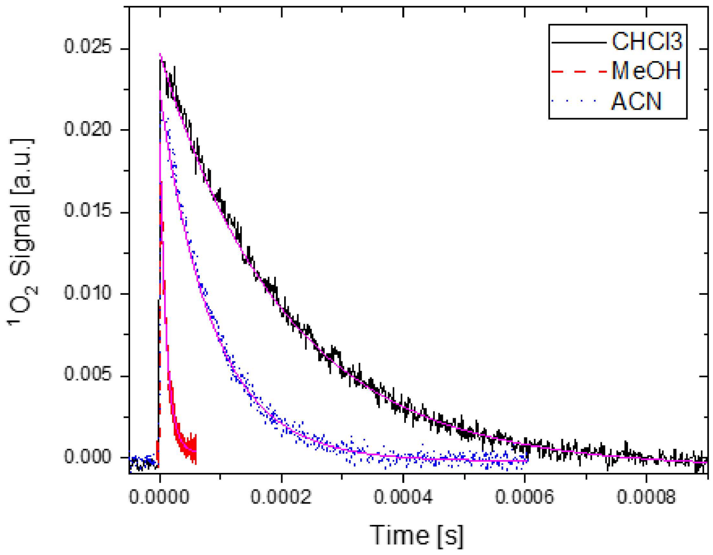

Figure E.2: Transient singlet oxygen luminescence of KA20-11H-proto in different solvents. The chlorin is excited at the Q-band. The concentrations are in the range 5 µM to 7 µM. The solid magenta lines are he single-exponential fits. The excitation wavelengths and resulting lifetimes for each solvent are presented in Table E.1.

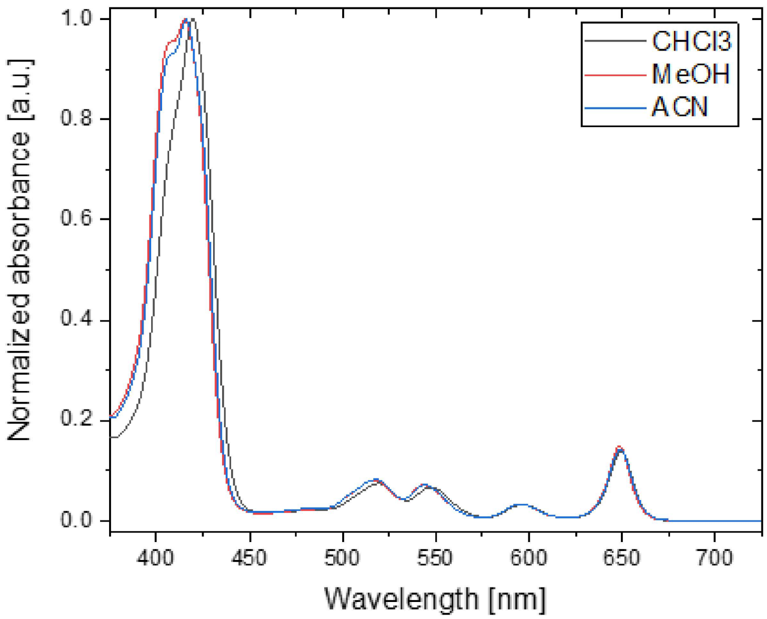

Figure E.3: Absorption spectra for KA20-11H-proto for different solvents.

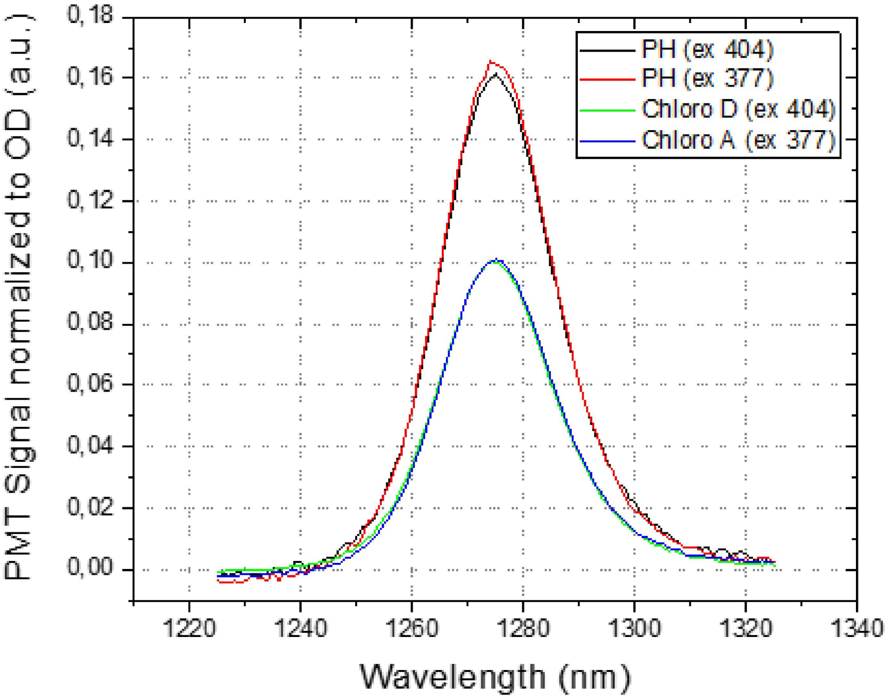

Figure E.4: Singlet oxygen emission spectra used to estimate the singlet oxygen quantum yield for KA20-15H (denoted "Chloro D") and KA20-15H-proto (denoted "Chloro A"). "PH" denotes phenantrone, the reference molecule. The singlet oxygen QYs for both chlorins were found to be 68 % (the same within experimental uncertainty).

Appendix F

Comparison of MTT and alamarBlue cell viability assays

Figure F.1 and Figure F.2 show the results of PDT experiments performed on AY27 cells incubated with the PS BAD-3 (10 µM). Figure F.1 shows results from a MTT assay, performed by S. Callaghan, University of Dublin. Figure F.2 show results from an alamarBlue assay performed as part of this project for the same PS, for the purpose of comparing the two assays.

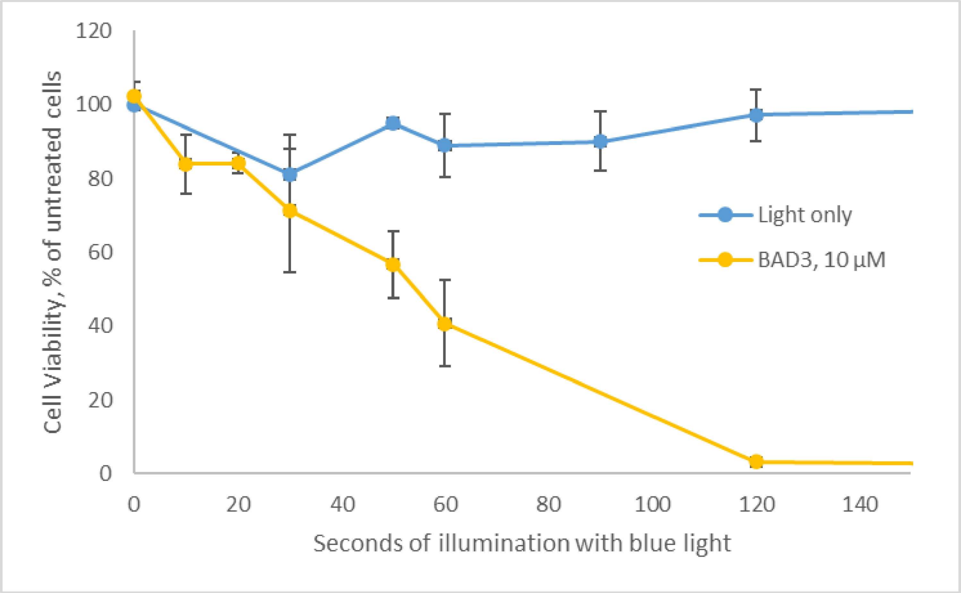

Figure F.1: MTT assay results for the relative cell survival of AY27 cells incubated with 10 µM of BAD3, compared to untreated cells. Courtesy of S. Callaghan, University of Dublin.

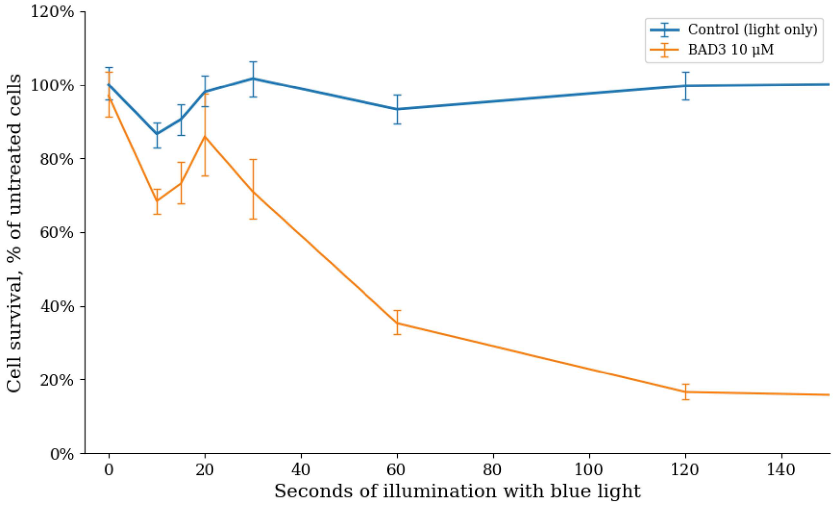

Figure F.2: AlamarBlue assay results for the relative cell survival of AY27 cells incubated 10 µM of BAD3, compared to untreated cells.

Appendix G

LumiSource® lamp

The spectrum of the PCI Biotech LumiSource® lamp was measured by a Jaz Spectrometer Module (Ocean Optics, USA) array spectrometer. The area-normalised spectrum is presented in Figure G.1, along with the area-normalised spectra of KA20-11H and KA20-11H-proto. The overlap percentages of the spectra were calculated to 8.1 % for KA20-11H and 7.4 % for KA20-11H-proto.

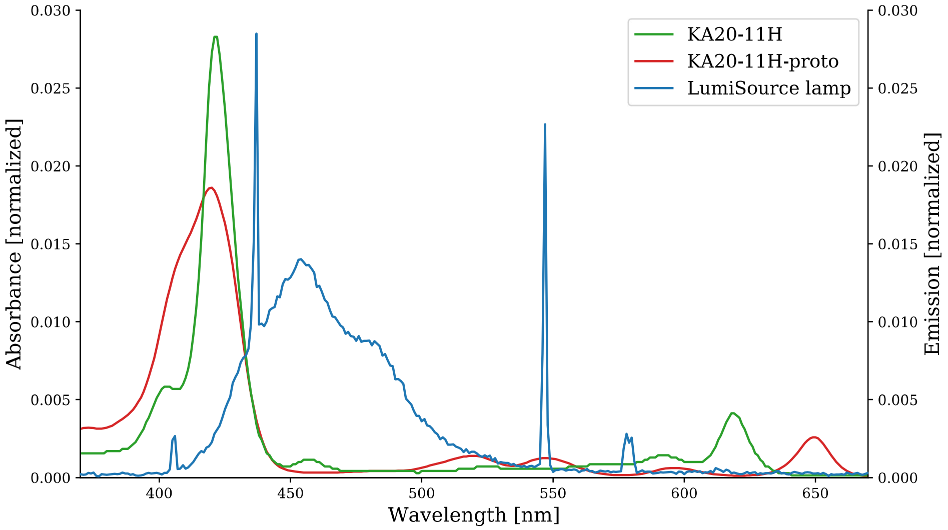

Figure G.1: Area-normalised emission spectrum of the LumiSource lamp and area-normalised absorption spectra of KA20-11H and KA20-11H-proto.

Benedikte Emilie Vindstad

Master's Thesis

NTNU
Norwegian University of
Science and Technology